ECS The Electrochemical Society
Advancing solid state & electrochemical science & technology

Review—Towards the Two-Dimensional Hexagonal Boron Nitride (2D h-BN) Electrochemical Sensing Platforms

Review—Towards the Two-Dimensional Hexagonal Boron Nitride (2D h-BN) Electrochemical Sensing Platforms

Shayan Angizi,[1] Maryam Khalaj,[2] Sayed Ali Ahmad Alem,[3] Amir Pakdel,[4] Magnus Willander,[5] Amir Hatamie,[5,6,7,z] and Abdolreza Simchi[7,8,z]

[1]Department of Chemistry and Chemical Biology, McMaster University, Hamilton, Ontario L8S 4M1, Canada
[2]Department of Materials Science and Engineering, Faculty of Engineering, Imam Khomeini International University, Qazvin, 34149-16818, Iran
[3]Department of Chemistry, Materials and Chemical Engineering, Politecnico di Milano, 20133, Milan, Italy
[4]School of Engineering, Trinity College Dublin, Lincoln Place, Dublin D02PN40, Ireland
[5]Department of Science & Technology, Linköping University, ITN-Campus, SE-60174 Norrköping, Sweden
[6]Department of Chemistry and Molecular Biology, University of Gothenburg, 41296 Gothenburg, Sweden
[7]Department of Materials Science and Engineering, Sharif University of Technology, Iran
[8]Institute for Nanoscience and Nanotechnology, Sharif University of Technology, 14588 Tehran, Iran

Electrochemical sensing performance of two-dimensional hexagonal boron nitride (2D h-BN) has traditionally been suppressed by their intrinsic electrical insulation and deficient electron transportation mechanism. However, the excellent electrocatalytic activity, high specific surface area, N- and B-active edges, structural defects, adjustable band gap through interaction with other nanomaterials, and chemical functionalization, makes 2D h-BN ideal for many sensing applications. Therefore, finding a pathway to modulate the electronic properties of 2D h-BN while the intrinsic characteristics are well preserved, will evolve a new generation of highly sensitive and selective electrochemical (bio)sensors. That is why extensive research has recently focused on the challenge to functionalize 2D h-BN by controlling the surface chemical reactions with external species, particularly metal nanoparticles. This review summarizes the most recent progress in the application of 2D h-BN nanosheets in electrochemical (bio)sensing. We will explore the fabrication techniques of 2D h-BN for electrochemical applications followed by thorough discussion on their advantages, shortcomings, and promising possibilities as (bio)sensing platforms in near future.

Revolution of graphene in 2004 and the massive incorporation of carbon-based nanomaterials into many applications, particularly in sensing areas, attracted the interest of academic societies into the alternative honeycomb structures.[1–5] Inspired by graphene, other 2D nanomaterials with single and multi-layer configurations have gained increasing attention, especially hexagonal boron nitride nanosheet, also known as "white graphene." Since then, we have witnessed the growing importance of 2D h-BN for a wide range of applications, from optoelectronic devices to electrochemical sensing platforms.[6–9] 2D h-BN is comprised of alternative boron (B) and nitrogen (N) atoms that are bound covalently (providing σ bonds) throughout a hexagonal structure with a highest occupied molecular orbital (HOMO) to lowest unoccupied molecular orbital (LUMO) gap of 5.1–5.9 eV, demonstrating electrical insulation.[10–14] Although it has been controversial whether this gap is direct or indirect in the last decade, most theoretical and experimental results have revealed the indirect transition of K (in valence) to M (conduction) in the band diagram.[15–17] Despite their large electronic band gap and insulation properties, the BN nanomaterials family are suitable for electrochemical applications due to their surface chemistry controllability, band gap tunability, high surface area and high catalytic activity.[18–20] Since the active layers of solid-state chemical sensors are required to be conductive enough to transport the charge carriers to gain final electrical signal, pure intact h-BN (either bulk or nanomaterials) may not be widely used directly and further subsequent chemical/physical surface modifications are necessary.[21,22] Hence, the fabrication technique of 2D h-BN sheets and their subsequent surface/edge functionalization are required to be well-controlled.

Lately, applications of 2D h-BN sheets in electrochemical sensors have gained attention due to their high surface area, active edges, low toxicity, and catalytic properties. Furthermore, feasible hybridization with other nanomaterials such as metal nanoparticles, can enhance their sensing performance against various chemical components as target analytes.[23] In addition, the nanosheets can be functionalized to enhance the sensors sensitivity and selectivity in electrochemical measurements.

In this regard, edge and surface functionalization, surface (in-plane) bearing of nanoparticles, and inducing structural defects are three main approaches for h-BN post-treatment.[24,25] For instance, hydroxylated edges of processed 2D h-BN sheets can modulate the band gap to as low as 3.5 eV.[26,27] Moreover, there are reports on amination,[28–30] fluorination,[31–33] as well as oxygen[25,34,35] and carbon[36–38] doping of h-BN to tune the properties. These functional groups can be enclosed to the 2D h-BN structure either during fabrication or later via surface modification methods. They provide the inert surface of h-BN with active sites that can interact with species selectively and more efficiently.[19,21]

Despite all recent publications on electrochemical (bio)sensing of h-BN, there has not been a comprehensive review on this topic yet. Herein, in the second chapter, we explain feasible synthesis methods of 2D h-BN to make them suitable for further sensing applications. In the third part, we review and summarize state of the art of 2D h-BN as a sensing platform. Finally, electrochemical applications with "analyte and mechanism" perspectives are elaborated. Figure 1 represents the schematics illustration of synthesis routes, surface modification and application of 2D h-BN, making them suitable for the electrochemical sensing performances.

Synthesis of 2D h-BN Sheets

It is well-known that the structural characteristics, properties, and ultimate performance of 2D h-BN nanomaterials strongly depend on their synthesis method. Generally, the synthesis routes of 2D materials can be classified into two major groups of top-down and bottom-up. Top-down approaches are ascribed as exfoliation procedures, having the bulk crystalline h-BN powder broken down to 2D h-BN using external chemical or mechanical forces, while
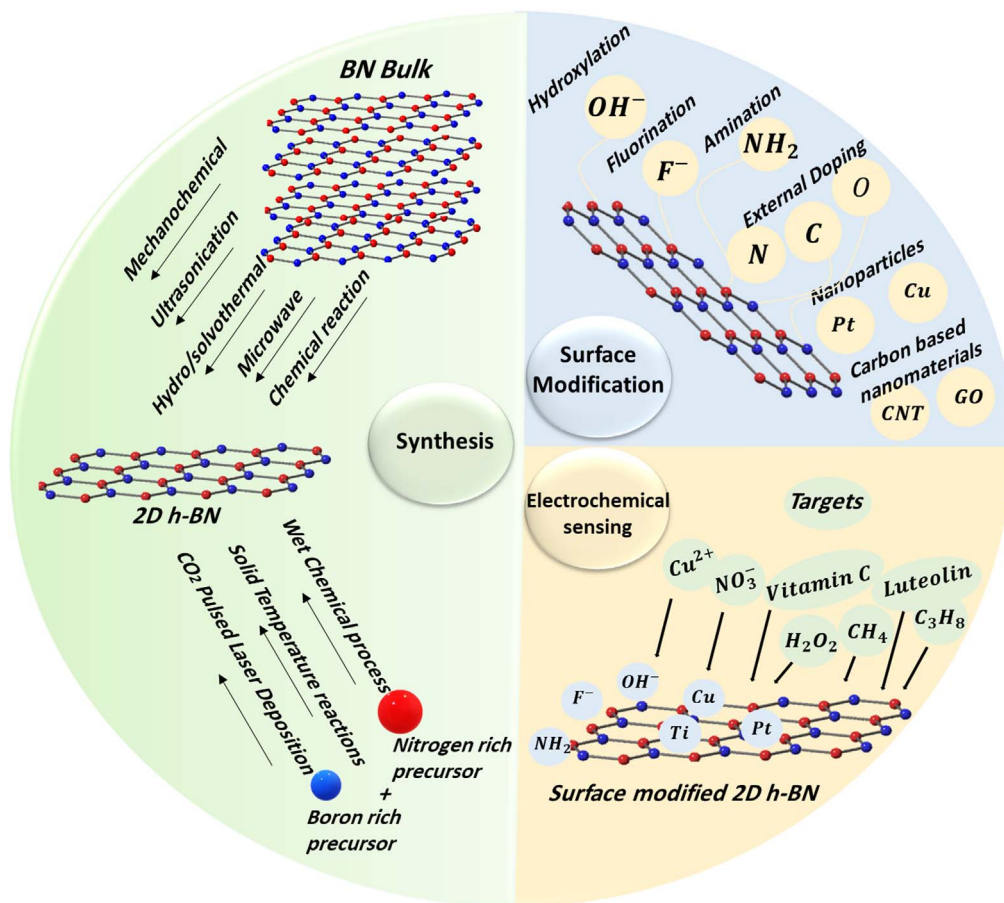
Figure 1. Schematic illustration of synthesis, surface modification, and electrochemical applications of 2D h-BN for detection of various analytes including ions and molecules.

bottom-up fabrication occurs through chemical interaction of boron and nitrogen-rich precursors.[39–41] In the following sections, we will discuss the efficient synthesis routes of 2D h-BN sheets which make them suitable for electrochemical sensing applications.

Top-down methods.— *Liquid-phase exfoliation.—*Exfoliation, in general, is a process in which the crystalline layered structure is transformed into single or few-layer nanosheets by breaking down the weak van der Waals interactions between the adjacent layers. Liquid-phase exfoliation refers to the process in which a liquid medium is involved. The required liquid medium can be either organic solvents such as N-methyl 2-pyrrolidone (NMP),[42] isopropyl alcohol (IPA),[40] ethylene glycol,[42] ethanol,[43] dimethylformamide (DMF)[44] or water.[45] In order to overcome the interlayer interactions in a liquid medium, different driving forces are employed including ultrasonication, chemical reactions, solvothermal, and microwave radiation to obtain well-dispersed and exfoliated 2D h-BN.[39,42,46] Although high crystalline 2D h-BN can be achieved in liquid-phase exfoliation, controlling the thickness, lateral size and the number of layers remains a challenge.[39]

*Ultrasonication assisted exfoliation.—*Ultrasonication exfoliation is a highly efficient and scalable method that has been extensively used for the production of 2D h-BN sheets in organic or aqueous solvents.[43] Due to pressure fluctuations arising from sonication bath, generation and collapsing of the bubbles within the liquid medium due to the "acoustic cavitation effect," triggers the exfoliation of h-BN layers. In addition, the "solvent polarity effect" joins the acoustic cavitation effect of sonication to render a complete exfoliation.[39,40] Yola et al.,[47–50] in their recent works, successfully prepared 2D h-BN by a simple ultrasonic exfoliation in IPA. For this purpose,

100 mg of h-BN powder was dispersed in 50 ml of IPA, then the suspension was heated at 50 °C for 24 h under vigorous stirring, prior to exposing to ultrasonic waves. Subsequently, ultrasonication was done for 20 h to delaminate the h-BN layers. Scanning electron microscopy (SEM) studies (Figs. 2a, 2b) revealed that the un-exfoliated (intact) BN has non-uniform morphology, different lateral sizes, and an agglomerated structure, while 2D h-BN exhibited reduced particle thickness and lateral sizes, confirming their successful exfoliation. As mentioned earlier, the chemistry of solvent considerably affects the product, so a smart systematic selection of solvent must be done for each individual process. For instance, it has been shown that exfoliation of h-BN powder in DMF through ultrasonication rendered high crystalline 2D h-BNs with distinct layers and the average sizes of 1 μm while there was no trace of a layered structure in pristine h-BN (Figs. 2c and 2d).[51] Moreover, the nitrogen adsorption-desorption studies and Brunauer–Emmett–Teller (BET) models of 2D h-BN confirmed the presence of mesoporous structure with a mean pore size of 2.90 nm.

Ultrasonication exfoliation can also be carried out in aqueous solutions without using any surfactants or auxiliary organic solvents; thereby, the pristine h-BN in this condition gets peeled off just by the aid of cavitation effect of sonication (Fig. 2e). The transmission electron microscopy (TEM) and high-resolution TEM (HRTEM) images of sonicated BN in water for 8 h[45] demonstrated that 2D h-BN possesses the thickness of 1.2–1.4 nm, equivalent to 3–4 atomic layers (Fig. 2f).

In general, in the presence of polar organic solvents, the exfoliation process can be attributed not only to the cavitation effect of ultrasonication but also to the strong interactions between the electric dipole of solvent molecules and locally polarized 2D h-BN. Albeit interaction chemistry of solvent will be discussed in the next
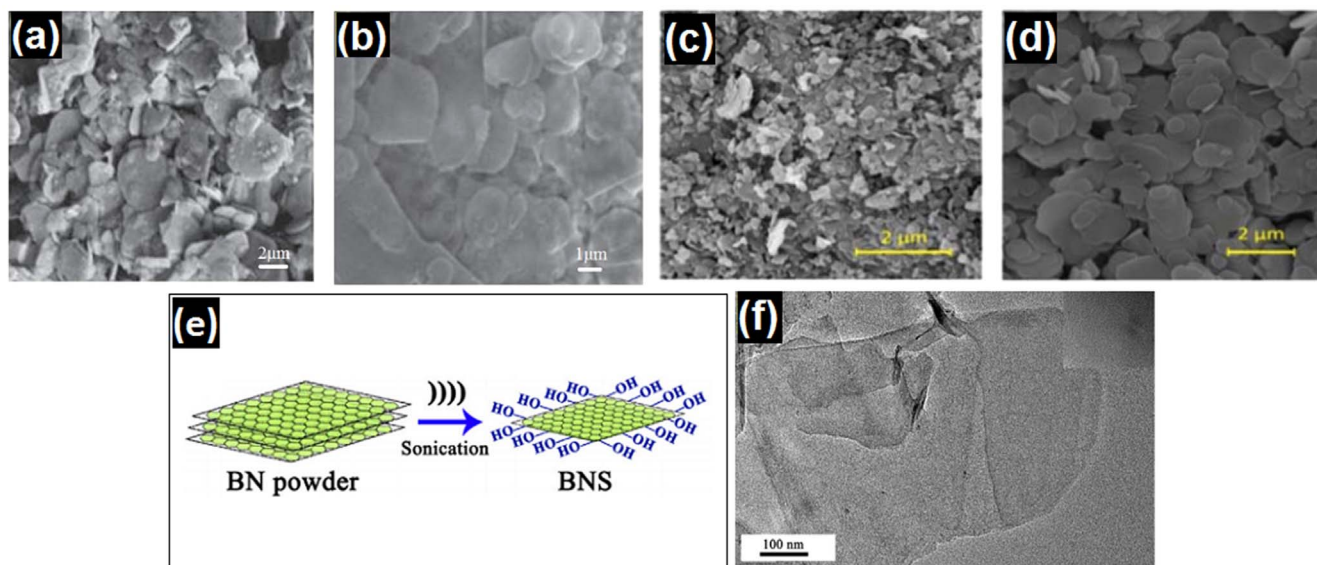
Figure 2. Ultrasonication-assisted liquid-phase exfoliation synthesis of 2D h-BN. SEM images of (a) bulk BN powder with irregular morphology and (b) exfoliated 2D h-BN with reduced lateral and particle size (Reprinted with permissions from IOP Publishing Ltd., Copyrights 2018; Elsevier, Copyrights 2018 and 2019).[47,50] SEM images of (c) pristine h-BN powder and (d) high crystalline, mesoporous 2D h-BN thin sheets with an average size of 1 μm (Reprinted with permission from IOP Publishing Ltd., Copyrights 2019).[51] (e) Schematic illustration of ultrasonication exfoliation of h-BN particles, (f) TEM and HRTEM (inset) images of 2D h-BN with 3–4 atomic layers and thickness of 1.2–1.4 nm (Reprinted with permission from Elsevier, Copyrights 2014).[45]

section, mainly atoms with high electronegativity such as oxygen (present on functional groups such as carbonyl, ester, ether and so on) may attack partially positive boron sites on the surface. These nucleophilic interactions minimize the energy at the materials edges. However, many interactions may happen in which nitrogen sites act as landing sites. Considering the Hansen solubility parameter (HSP) theory and Coleman theoretical calculations (Hansen-Coleman model), which is mainly focused on optimization of interactions and binding energies between the solvent and solute, proper solvents for dispersion of 2D h-BN are those that reduce the enthalpy of the overall mixture, which eventually minimize the exfoliation energy. Therefore, when the surface tension energy of the selected solvent is close to the surface tension energy of the 2D h-BN ($\sim$65 mJ m^{-2} [42]), the required energy for exfoliation reduces and leads to overcoming the van der Waals force between two sequential layers. Concerning this, IPA and NMP solvents can be potentially suitable candidates for ultrasonic exfoliation of bulk h-BN.[40,42,52] However, without using any organic solvents or surfactants, exfoliation of h-BN can also be successfully done in water to exploit the sonicated-assisted hydrolysis. Like organic solvents, the polarity effect of water merges with the cavitation effect of sonication to deliver well-exfoliated 2D h-BN.

However, the obtained impurity-free 2D h-BN has reduced lateral sizes as a result of sonicated-assisted hydrolysis. This weakness can be surmounted by the incorporation of surfactants to the aqueous solution to improve the dispensability and final structural properties of the 2D h-BN, although it blocks the electrocatalytic active spots or metal-anchoring sites.[40,43,53] Eventually, in comparison to the aqueous medium, organic solvents are more efficient in delivering well-dispersed, highly exfoliated 2D h-BN ultrathin nanosheets and hence higher surface area, which make them more promising for sensor applications.[53]

Microwave-assisted exfoliation.—Besides sonication, alternative driving forces such as microwave irradiation have been widely used to exfoliate layered structures. However, unlike ultrasonication which is often a time and energy-consuming process, microwave exfoliation allows fast production of 2D h-BN in a facile, green, and low-cost way. Generally, the high energy dielectric heating of microwave radiations decreases the kinetic potential of chemical reactions and the overall reaction time needed for exfoliation and

conversion of bulk BN directly to 2D h-BN on the scale of minutes.[39,54] The microwave irradiation provides the energy for solvent molecules to be embedded between/into the h-BN layers and act as spacers. It also facilitates intercalation caused by solvent/BN interactions.[55]

Since microwave radiation as the heating source is stable during the exfoliation process, the microwave absorption capacity of the exposed materials determines the quality of the final product. Chemical composition, especially the quantity of oxygen-containing groups, strongly affects the microwave absorption capacity. Due to the absence of oxygen-containing groups in 2D h-BN structure and its high thermal conductivity, it easily absorbs the high energy dielectric heating of microwave radiations and disseminates it through the molecular level to render swift thermal exfoliation.[56–58]

In 2018,[59] microwave irradiation was utilized as a swift driving force to exfoliate microwave susceptors (h-BN particles). For this purpose, the mixture of h-BN, ethanol, and NaOH (0.5 g, 100 ml, and 1 M, respectively) was initially sonicated and then the sealed suspension was transferred to a household microwave oven (800 W) and subjected to microwave irradiation for 2 min. Finally, the 2D h-BN with good quality and high surface area were obtained. In this case, Na$^+$ and OH$^-$ ions were embedded within the layers of h-BN and 2D h-BN were functionalized with the hydroxyl group.

Chemical reaction-assisted exfoliation.—Chemical reaction-based exfoliation is considered as a straightforward and cost-effective driving force that can trigger the production of 2D h-BN. This technique does not require elevated temperatures or high vacuum, as it is based on wet chemical processing at around room temperature. During this process, formation of chemical compounds as a result of sequential chemical reactions between the starting materials ultimately lead to breaking the weak van der Waals force between the adjacent h-BN layers.[6,60] For example, Adeel et al.[61] exfoliated 2D h-BN sheets through the following protocol: 2 g h-BN powder was stirred in 50 ml of H$_2$SO$_4$ solution for 30 min. Then, the suspension was transferred to an ice bath prior to gradually adding 1 g of KMnO$_4$ and kept the suspension in stirring for 12 h. Afterward, 10 ml of H$_2$O$_2$ (30%) was added to the as-made suspension and stirred for another 5 h. The underlying exfoliation mechanism was attributed to three main steps (Fig. 3a): (1) h-BN powder was mixed with H$_2$SO$_4$; the H$^+$ ions of the sulfuric acid were incorporated
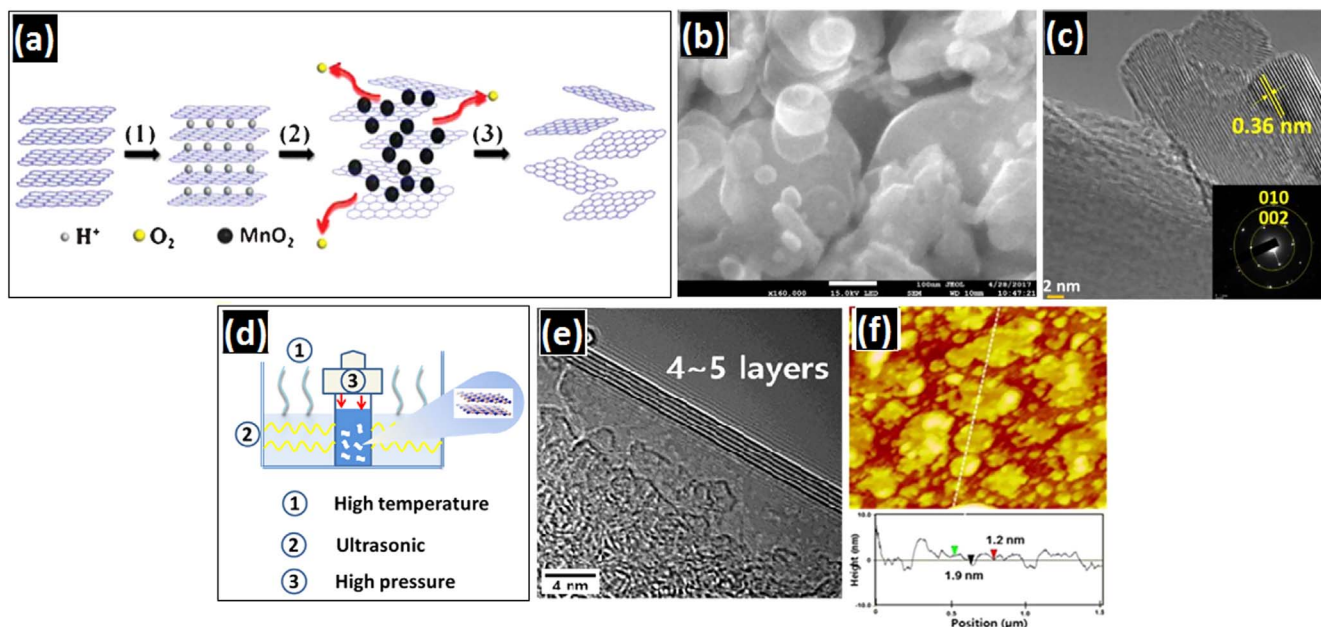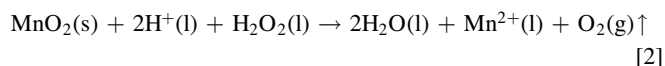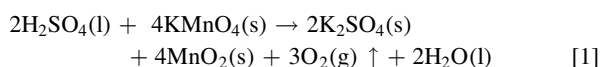
Figure 3. Chemical reaction and hydrothermal/solvothermal-assisted liquid-phase exfoliation of 2D h-BN. (a) Schematic illustration of the chemistry behind chemical reaction-assisted exfoliation (Reprinted with permission from the Royal Society of Chemistry, Copyrights 2013).[60] (b) SEM and (c) HRTEM images (inset: selected area electron diffraction (SAED) pattern) of high crystalline 2D h-BN thin nanosheets obtained from chemical reaction exfoliation with the interlayer spacing of 0.36 nm (Reprinted with permission from Elsevier, Copyrights 2019).[61] (d) Schematic illustration of hydrothermal/solvothermal-assisted exfoliation (Reprinted with permission from Springer, Copyrights 2019).[62] (e) HRTEM and (f) AFM images of solvothermal exfoliated 2D h-BN thin nanosheets with the thickness of 1.2–1.9 nm and 4–5 atomic layers (Reprinted with permission from Elsevier, Copyrights 2018).[29]

within the layers of h-BN sheets as spacers and increased their interlayer distances, (2) the added KMnO₄ reacted with H₂SO₄, resulted in the formation of MnO₂ nanoparticles (NPs) (reduction of Mn^{+2}), which further enhanced the interlayer gap (Eq. 1). MnO₂ NPs disturbed the long-range order of the h-BN sheets and inhibited their re-stacking. (3) Lastly, the reaction happening between the added H₂O₂ and MnO₂ NPs resulted in the formation of O₂ gas (Eq. 2), which provided the final repulsive force to overcome the interactions. The following equations summarize the sequential chemical reactions that led to exfoliation[60]:

$$2H_2SO_4(l) + 4KMnO_4(s) \rightarrow 2K_2SO_4(s)$$
$$+ 4MnO_2(s) + 3O_2(g) \uparrow + 2H_2O(l) \qquad [1]$$

$$MnO_2(s) + 2H^+(l) + H_2O_2(l) \rightarrow 2H_2O(l) + Mn^{2+}(l) + O_2(g)\uparrow$$
$$[2]$$

The obtained 2D h-BN sheets were highly exfoliated, transparent to electron beam, and well crystalline (Figs. 3b and 3c). The interlayer spacing between the sheets was measured to be ∼0.36 nm.

Hydrothermal/solvothermal-assisted exfoliation.—Hydrothermal/ solvothermal-assisted exfoliation is frequently used to deliver well-exfoliated 2D h-BN sheets. "Hydro" and "solvo" refer to the existence of aqueous and organic solvents, respectively and "thermal" shows the existence of a fairly high temperature. This process is accompanied by ultrasonication and requires heating the mixture of h-BN bulk powder and a solvent in specific concentration in a sealed Teflon capped autoclave. As temperature and consequently pressure go up, either solvent molecules or generated ions (as a result of self-dissociation of liquid medium) act as spacers and increase the interlayer distance between the h-BN sheets (Fig. 3d).[62,63] Generally, almost all the liquid-phase exfoliation methods are accompanied by high-energy sonication; thus, they are unable to deliver large lateral sizes of 2D h-BN sheets.[40,62]

Recently, exfoliated 2D h-BN sheets were prepared by H₂O₂ treatment through a surfactant-free hydrothermal reaction.[43,64] For

this purpose, 150 mg of h-BN powder was ultrasonicated in 30 ml of H₂O₂ (30%) as an inorganic reagent within a Teflon-coated autoclave for 15 min. Then, the hydroxylated h-BN suspension was transferred to a thermostated water bath at 80 °C for 20 h. After the autoclave treatment, the resulting suspension was centrifuged, washed and dried to obtain 2D h-BN sheets which were more chemically active for post-treatment. TEM images confirmed thin sheets of 2D h-BN with sizes of several hundred nanometers.

In another study,[29] pre-treated BN powder in an acidic mixture (H₂SO₄:HNO₃ = 3:1) was solvothermally exfoliated in an organic solvent (oleylamine). Then, the suspension was transferred to a sealed reactor container, heated to 170 °C for 48 h, and sonicated for 30 min. The obtained 2D h-BN containing suspension was centrifuged and dried to render 2D h-BN sheets in powder form. The morphological observations and atomic force microscopy (AFM) image (Figs. 3e and 3f) determined a 300 nm average size with thickness of 1.2–1.9 nm, corresponding to 4–5 atomic layers.

Mechanochemical exfoliation of h-BN particles.—Mechanical milling with/without a liquid medium (wet/dry process, respectively) has been introduced in the last decade to obtain highly exfoliated h-BN. The wet medium acts as a lubricant against h-BN particles and inhibits their re-welding. During the milling process, a mild shear force is generated which triggers the exfoliation by overcoming the weak van der Waals interactions between the h-BN layers (Fig. 4a)[56]. In addition, this method benefits from the solvent polarity effect of the wet medium, shear force of milling, and shear force of solvent due to the gravitational forces to render well-exfoliated 2D h-BN sheets. Furthermore, the type and size of the used balls in the milling process, the time of milling, and the selection of a proper wet medium as a lubricant are decisive parameters on the exfoliation process quality.[40,42,46] An efficient milling process requires: (1) small-sized milling media and balls to increase the milling action and decrease the potential damage, and (2) selection of matching solvent which has similar surface energy as h-BN sheets. Generation of exfoliated 2D h-BN with low defect density and high crystallinity, and almost the same lateral sizes of their un-exfoliated h-BN crystals are among the advantages of this method, making it a high yield approach.[40,42]
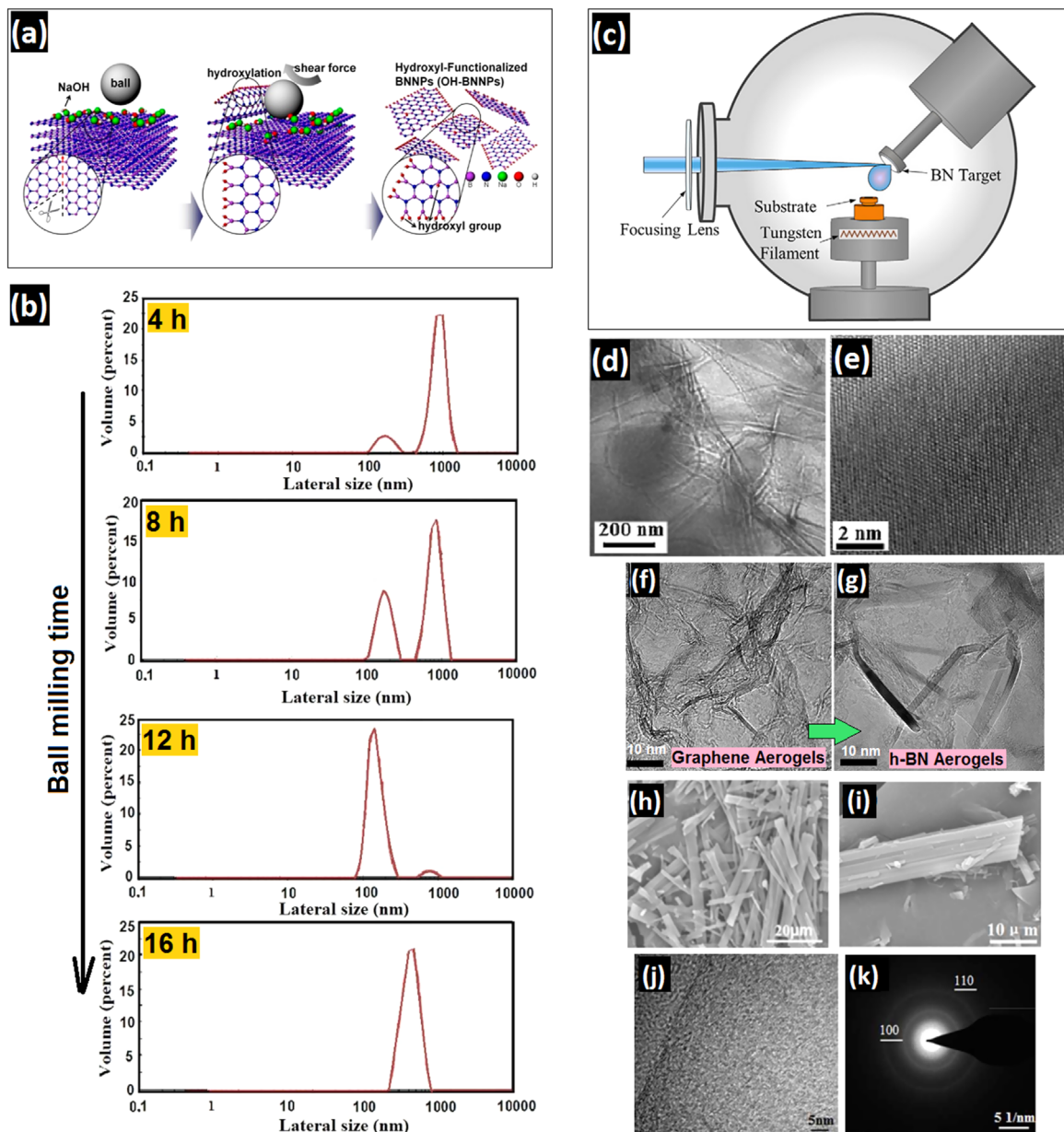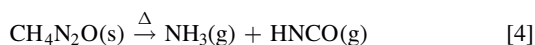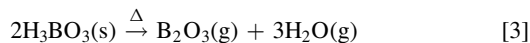
Figure 4. Mechanochemical exfoliation, CO_2-pulsed laser deposition and High-temperature solid-state synthesis of 2D h-BN. (a) Illustration of surface chemistry of mechanochemical exfoliation of h-BN powders (Reprinted with permission from MDPI, Copyrights 2019),[56] (b) dependency of the size distribution of h-BN particles on the time of ball milling (Reprinted with permission from American Chemical Society, Copyrights 2018).[65] (c) Schematic representation of CO_2-pulsed laser deposition technique for 2D h-BN sheets formation (Reprinted with permission from Elsevier, Copyrights 2014),[66] (d) TEM and (e) HRTEM of the deposited high crystallinity 2D h-BN sheets (Reprinted with permission from Elsevier, Copyrights 2014).[67] HRTEM images of (f) graphene aerogels and (g) h-BN aerogels converted from graphene aerogels by the carbothermal method (Reprinted with permissions from American Chemical Society, Copyrights 2013).[68] (h)–(k) SEM, TEM and SAED pattern images of the poorly crystallized h-BN whickers, obtained from pyrolization of a polymeric precursor, with 50–200 nm in length and 0.5–3 μm in thickness (Reprinted with permission from the Royal Society of Chemistry, Copyrights 2016).[69]

Recently, we reported[65] the fabrication of 2D h-BN sheets through a mechanochemical protocol, using ethanol as a wet medium due to its suitable polarity (4.3), facile removability, low toxicity, and sufficient surface energy to peel off the layers. Time optimization using dynamic light scattering (DLS) demonstrated a size dependence of 2D h-h-BN particles on ball milling duration (Fig. 4b). The amount of smaller exfoliated particles increased up to 12 h of milling where almost all the grounded particles were ultrafine (150 nm). However, continuing the ball milling after 12 h had a negative impact and led to the sticking of the ultrafine particles and resulted in coarser sizes. At least 4 h and at most 12 h were required to render efficiently exfoliated 2D h-BN particles.

Bottom-Up methods.—Bottom-up approaches in the synthesis of 2D h-BN sheets refer to reactions between boron and nitrogen-containing precursors such as melamine ($C_3H_6N_6$), urea (CH_4N_2O), diboron trioxide (B_2O_3), boric acid (H_3BO_3), and ammonia gas (NH_3)[42] through chemical vapor deposition (CVD), solid-state reactions, wet chemical synthesis, and pulsed laser depositions.

Wet chemical synthesis.—Wet chemical syntheses include a broad variety of methods such as solvent evaporation, hydro-thermal/solvothermal, and template-assisted routes.[39] As an example,[70] the chemical reaction between boric acid (H_3BO_3) and urea (CH_4N_2O), as boron and nitrogen-rich precursors, respectively,

fabricated 2D h-BN sheets by a chemical wet approach. For this purpose, a mixture of boric acid and urea (1:24) was ultrasonicated and the dried product was exposed to 950 °C in N_2 atmosphere for 5 h to obtain 2D h-BN sheets. The following sequential chemical reactions suggest the formation mechanism of 2D h-BN sheets[71]:

$$2H_3BO_3(s) \xrightarrow{\Delta} B_2O_3(g) + 3H_2O(g) \qquad [3]$$

$$CH_4N_2O(s) \xrightarrow{\Delta} NH_3(g) + HNCO(g) \qquad [4]$$

$$B_2O_3(g) + 2NH_3(g) \xrightarrow{\Delta} 2BN(s) + 3H_2O(g) \qquad [5]$$

CO$_2$-pulsed laser deposition (CO$_2$-PLD).—Pulsed laser deposition (PLD) is a substitute method for physical vapor deposition (PVD) technique. Due to the pressure difference of elements in the vapor phase, PVD is not an efficient method to form complex stoichiometric films; however, owing to localized, fast heating, and the generation of stoichiometric plasmas, PLD is capable of producing crystalline complex thin films. Briefly, in PLD, a target surface is subjected to a high energy laser beam (Figs. 4c) to form a plasma plume of the target composition. The generated plasma plume moves toward the substrate surface and deposits to form the film. The final quality of the generated film depends on many parameters including pulse rate and duration, laser energy, the distance of the target to the substrate and their orientations. The high energy CO_2 beam ($\lambda \sim 10{,}600$ nm) can also be considered as a focused laser beam for pulsed-laser deposition.[66,72–74] For this purpose, Sajjad et al.,[67] deposited 2D h-BN sheets on a silicon substrate by irradiating a pyrolytic h-BN target with CO_2 laser pulses. The silicon wafer (Si 100) was initially washed in acetone and methanol then heated up to 400 °C. Silicon substrate and pyrolytic h-BN target were 3 cm apart and the CO_2 laser beam irradiated the h-BN target under high vacuum to eventually deposit 2D h-BN sheets on the silicon substrate. The film formation mechanism is as following: the generated plasma plume out of pyrolytic h-BN target consist of high energy B^+ and N^- ions in a gaseous state, and when they hit the hot surface of Si substrate, the extra thermal energy provided from substrate leads to the collision of those ions and grow a small h-BN layer, which is merged into 2D h-BN sheets parallel to the substrate surface. According to the morphological characterizations (Figs. 4d and 4e), the deposited 2D h-BN sheets overlapping each other possess ordered B and N atoms throughout a 2D honeycomb crystal lattice.

High-temperature solid-state synthesis.—Similar to the wet chemical processes, high-temperature solid-state interactions between boron and nitrogen-rich precursors can cause a series of chemical reactions to deliver 2D h-BN sheets. However, the reaction temperature is fair that no liquid medium exists. In fact, elevated temperatures transform solid materials to their gaseous states and provide enough vapor pressure for their efficient reaction to reach high purity 2D h-BN sheets. However, exposure to high temperatures and various flowing gasses can induce defects in the structure of the final product. Optimistically, the defects introduce new mid-bands near the HOMO or LUMO band edges which improve the near-band edge transitions of electrons and act as active sites to assist the electron transfer, which leads to facilitated electrochemical reactions and sensing performances.[40]

2D h-BN aerogels due to their exceptional structural characteristics including high surface area and low density can be obtained from nontoxic and nonhazardous reactants like graphene aerogels. Recently, high crystalline, high surface area, and mesoporous 2D h-BN aerogels were synthesized using graphene aerogels as precursors[75] through carbothermal reduction of diboron trioxide (B_2O_3) in the presence of N_2 atmosphere at 1600 °C–1800 °C. For this purpose, graphene aerogels and B_2O_3 were placed in a graphite crucible and exposed to a high temperature under the flow of N_2 gas. At about 1600 °C–1800 °C, the solid-state reaction between the three components (Eq. 6) led to the formation of pure 2D h-BN aerogels. In fact, B_2O_3 is in vapor phase at temperatures above 1500 °C and can get into reaction with nitrogen gas to produce 2D h-BN sheets. It is worth mentioning that the obtained h-BN aerogels consist of 2D h-BN sheets connected in a 3D network. The following equation explains the mechanism behind the production of 2D h-BN aerogels from graphene[68]:

$$B_2O_3(s) + N_2(g) + 3C(s) \rightarrow 2BN(s) + 3CO(g) \qquad [6]$$
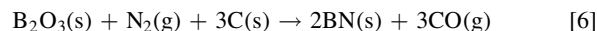
According to morphological images (Figs. 4f and 4g), the resulting 2D h-BN aerogels possess ultrathin, wrinkled sheets and have higher crystallinity and order upon conversion from graphene aerogel.

In another study, Luo et al.[69] managed to synthesize 2D h-BN whiskers from a polymeric precursor, the mixture of boric acid (H_3BO_3) and melamine ($C_3H_6N_6$), under nitrogen-rich atmosphere at elevated temperatures. For this purpose, the polymeric precursor solution was first prepared by 3:1 molar ratio of H_3BO_3:$C_3H_6N_6$, using a wet chemical method. Then the obtained solid N and B-rich precursor was heated to 800 °C–1000 °C for 3–5 h under flow of forming gas (5% hydrogen). SEM images revealed the poor crystallinity and defective structure of 2D h-BN whiskers (with 0.5–3 μm in diameter and 50–200 μm in length) (Figs. 4h–4k). In addition, BET model calculated a surface area of 964.3 m^2 g^{-1}, confirming the presence of micropores and mesopores on the synthesized whiskers. Similarly, Shen et al.[76] fabricated 2D h-BN via one-step calcination using melamine borate ($C_3H_6N_6$.x H_3BO_3) as a single precursor. To prepare melamine borate, 4 g of melamine ($C_3H_6N_6$) was dissolved in 85 °C water, and 1 g of boric acid (H_3BO_3) was added to the as-made solution and stirred for 1 h. Then, the final precursor mixture was obtained after filtering and drying the above solution. At last, the mixture was heated up to 900 °C for 4 h under a reducing atmosphere to obtain defect-rich 2D h-BN. The TEM observations revealed the layered structure of the as-obtained 2D h-BN with ample pores on their surface, as a result of gas emission during pyrolization. Accordingly, BET model depicted that the high surface area of 198.41 m^2 g^{-1} of the product can be attributed to its porous structure as a result of pyrolization. In the next study,[77] the solid-state fabricated 2D h-BN exhibit exceptional electrocatalytic properties. For this purpose, a 10:7 weight ratio of anhydrous borax (B_2O_3) and melamine ($C_3H_6N_6$) was ball milled and the grounded product was heated at 300 °C for 2 h in air. Then, it was calcinated at different temperatures: 700 °C for 1 h, 800 °C for 1 h, and 900 °C for 2 h, under N_2 atmosphere. The calcinated product was washed and filtered to isolate the unreacted precursor before drying the final 2D h-BN product. The produced 2D h-BN nanostructures were very thin, transparent to electron beam, and well-crystallized. In addition, the large numbers of open edges were considered as electrocatalytic active sites to improve electrochemical properties.

2D h-BN Sheets-Based Electrochemical (bio)Sensors

Over the last decade, outstanding chemical and optoelectrical properties of h-BN nanomaterials[78–82] have led them to pave new paths in a wide range of applications including on-off probes,[83] electrochemical sensors,[7] electrochemiluminescence applications,[30,84] bioimaging techniques,[85] photocatalytic applications,[81] and cancer therapy.[79] Unlike other famous layered structures such as graphite or molybdenum disulfide (MoS_2) which are either fully conductive or semi conductive, partially covalent bonds between B and N atoms disturb the electronic states symmetry through narrowing the sp^2-derived π bands and generate a large band gap ($\sim$5.1–5.9 eV[6,40]) in h-BN. Therefore, the electrically insulating h-BN has found limited electrochemical sensing applications.[39,40,86] However, innovating strategies to modulate its electrical properties to meet
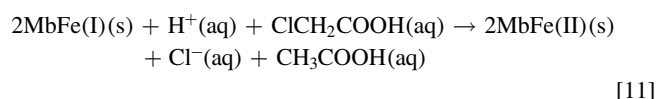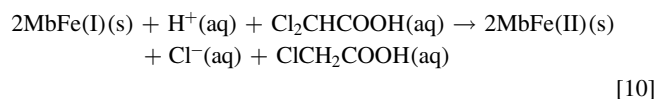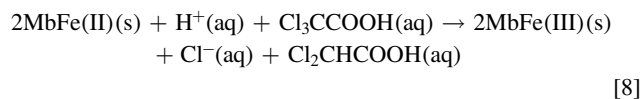
essential requirements for functional electronic applications have been the matter of focus for researchers to exploit the full potential of this material. There are common techniques to manipulate h-BN sheets' large band gap such as basal plane and edge functionalization, atom doping, hybridization with graphene, and various defect types including atomic vacancies, grain boundaries, step edges and corners, and substitution atoms which engender local effects that result in a reduced band gap, tuning h-BN for highly catalytic sensing and charge storage applications.[39,40,46,86,87] Therefore, the high surface area alongside with adjusted electroconductivity makes h-BN an attractive nomination for electrochemical sensing platforms. Meanwhile, careful discussion on the advantages of 2D h-BN compared with other analogous layered structures such as graphene is important to point out. Herein, different features should be taken into account. From the electrical conductivity point of view, the electrical insulation may suppress the sensitivity of the 2D h-BN based sensors, however, their high chemical stability would provide better stability and lower current drifting over time along with better cost-effectivity. On the other hand, atomic diversity on the BN surface (B and N) compared to graphene (only C) gives a great opportunity for smart functionalization (physical or chemical) through different surface treatments. Moreover, the capability of bandgap tuning (reduction) from 5.9 eV (bulk) down to 0.78 eV (reported for defective –OH terminated boron nitride quantum dots[26]) will make them excellent candidates for a range of applications. While the bandgap enlargement of graphene is often limited by the appearance of high asymmetry in electronic band structure leading to subsequent restrictions of their functionality.[88] Furthermore, BN is an exciting alternative to graphene-based materials when the biocompatibility matters the most. In fact, unlike graphene where the lateral size, synthesis approach, operational conditions determine the toxicity or bio-compatibility, BN itself having no coatings can be bio-compatible in vitro and in vivo. This assists BN nanomaterials to not exhibit toxic effects in contact with living systems and makes them promising candidates for many bio applications from bioimaging, cancer therapy to electrochemical bio sensors.[89] In the following sections, we provide an overview of the recent advances on 2D h-BN sheets for electrochemical (bio)sensing applications listed in Table I.

Pristine 2D h-BN used for electrochemical sensors.—Despite the wide band gap and electrical insulation of h-BN, pristine 2D h-BN can act as a potential electrocatalyst for detection of various types of ions and/or molecules. For instance, in 2018, a drop cast 2D h-BN quantum dots (BNQDs) on gold screen-printed electrode (GSPE) was fabricated for vitamin C ($C_6H_8O_6$) detection in commercial drinks (orange and lemon juices).[65] Vitamin C plays a critical role in the well-functioning of the immune system and is omnipresent in variety of food and drug products.[95,96] Thereby, its selective detection is very important. The electroanalytical vitamin C sensing property of the BNQT/GSPE through CV examinations in Fig. 5a exhibited significant decrease in peak potential of vitamin C (∼0.37 V) compared to un-modified gold electrode, which confirmed the electrocatalytic activity of BNQDs on the gold substrate. This decrement may stem from two main reasons: (1) the adsorption of vitamin C probably occurred from their O sides by the catalytic active spots of h-BN, and (2) the high surface energy BNQDs might reduce their energy through surface adsorption of vitamin C. This ameliorated electrocatalytic performance with high sensitivity and low limit of detection (LOD) 0.45 μM originated from the local interaction between N-p_z and B-p_z orbitals of 2D h-BN and d_z^2 orbitals of the gold substrate.[86,97,98]

In a similar work, a screen-printed graphitic electrode (SPE) modified by drop-cast 2D h-BNs was utilized for detection of dopamine (DA, $C_8H_{11}NO_2$) in biological samples.[23] As DA coexists with ascorbic acid (AA) in a variety of biological samples, their redox peaks might overlap with each other, making it difficult to differentiate them. The higher anodic peak current of bare SPE electrode at 0.37 V compared to glassy carbon electrode (GCE) and boron-doped diamond (BDD) in Fig. 5b clearly indicated the highly sensitive electrocatalytic detection

(LOD = 0.65 μM) of DA. When SPE is modified with different mass loadings of 2D h-BNs, it successfully detects DA by showing an increment in anodic peak current while a decrease in its correspondence voltage (Fig. 5c). Also, the fabricated sensor showed good selectivity and was capable of simultaneous detection of DA and AA (LOD = 0.65 μM for DA), as demonstrated in Fig. 5d. The 2D h-BNs assist to distinguish the required oxidation potential of DA and AA significantly so that no overlap was perceived.

In another work,[69] poorly crystalline h-BN whiskers with high defect density were coated on a Ti substrate to construct a new platform to oxidize and detect nitrite ions (NO_2^-) in tap water samples (Fig. 6a). CV examinations in Fig. 6b confirmed the appearance of an intense anodic oxidation peak in the h-BN whiskers/Ti electrode at 0.94 V which is a manifestation of nitrite oxidation, confirming the effective sensitivity of the electrode in the trace amounts of nitrite species. The superb electrochemical sensing of the h-BN whiskers originated from its micro/mesoporous structure and high defect density which provided high pore volume and multiple active sites that act as enhanced nitrite receptors. Therefore, these high-energy adsorption sites led to swift electron transportation, resulting in high sensitivity and selectivity of the fabricated sensor with LOD 0.089 μM and linear ranges of 10–400 and 400–6300 μM. This has been followed by a recent research reporting a novel electrochemical sensor made by Nafion/myoglobin (Mb)/2D h-BN/ionic liquid modified carbon paste electrode (CILE) for detection of trichloroacetic acid (TCA, $C_2HCl_3O_2$) in drinking water (Fig. 6c).[92] Detection of TCA requires Mb as an intermediate redox protein for electrocatalytic sensing and the underlying catalytic property of Mb originates from the presence of iron ions (Fe^{3+}) in the depth of its molecular structure. Therefore, the high specific area of 2D h-BN bridged the distance between the Mb's electroactive center and the surface of electrode to facilitate electron movement. Besides the electrocatalytic TCA sensing of the electrode, its superior electrochemical behavior was authenticated by CV technique (Fig. 6d). Due to the appearance of two quasi-reversible redox peaks, wider integrated area, and higher redox peak currents of the modified electrode, the electrochemical performance outstripped the bare electrode. These results could be attributed to the electroactivity of Mb that is enhanced by h-BN and their efficient cooperation in accelerating the electron transfer.[99,100] Electrocatalytic sensing response of the Nafion/Mb/h-BN/CILE electrode in tap water with various concentrations of TCA (from 0.2 to 30 mM) showed two cathodic reduction peaks as a result of reduction of Mb in the presence of TCA (Fig. 6e). The two cathodic peaks were located at −0.355 and −0.551 V; the former is assigned to the reduction of MbFe(III) → MbFe(II) and the latter to the reduction of MbFe(II) → MbFe(I). The sequential electrocatalysis reactions occurred according to the following equations[92]:

$$MbFe(III)(s) + e^- \rightarrow MbFe(II)(s) \quad [7]$$

$$2MbFe(II)(s) + H^+(aq) + Cl_3CCOOH(aq) \rightarrow 2MbFe(III)(s) + Cl^-(aq) + Cl_2CHCOOH(aq)$$
$$[8]$$

$$MbFe(II)(s) + e^- \rightarrow MbFe(I)(s) \quad [9]$$

$$2MbFe(I)(s) + H^+(aq) + Cl_2CHCOOH(aq) \rightarrow 2MbFe(II)(s) + Cl^-(aq) + ClCH_2COOH(aq)$$
$$[10]$$

$$2MbFe(I)(s) + H^+(aq) + ClCH_2COOH(aq) \rightarrow 2MbFe(II)(s) + Cl^-(aq) + CH_3COOH(aq)$$
$$[11]$$

Focusing on simultaneous catalytic sensing, a recent study[76] took advantage of electroactive nature of phenol (Ph, C_6H_6O) and its derivative 4-aminophenol (4-AP, C_6H_7NO) to develop a new defect-

Table I. Electrochemical sensing properties of 2D h-BN-based ion/molecule/gas sensors.

Modified Electrode	Analyte (s)	Detection Environment	Role of 2D h-BN	Linear Range	LOD	References
2D BNQDs[a)]/GSPE[b)]	Vitamin C	Commercial drinks (orange and lemon juices)	High electrocatalytic activity for oxygen reduction reactions owing to the interaction between the N-p_z and B-p_z orbitals	0.80–5.0 mM	0.45 μM	65
MIP[c)]/BNQDs/GCE[d)]	Cardiac Troponin-I	Plasma samples	Providing a high surface area, facilitated electron transfer, and biocompatibility	0.01–5.00 ng ml^{-1}	0.0005 ng ml^{-1}	90
BNQDs/GO[e)]/GCE	Organophosphate pesticides	water and apple juice	Decreasing mass resistance and accelerated electron transfer	0.31–0.067 pM	0.0033 pM	91
2D h-BN/SPE	DA[f)]	Not mentioned	Effective electrocatalyst in the simultaneous detection of DA and UA	Not mentioned	0.65 μM	23
2D h-BN whiskers/Ti	Nitrite ion	Tap water	Providing a high surface area and void volume with high density defects and porous structure	10–400 and 400–6300 μM	−0.089 and −0.412 μM	69
Cu NPs[g)]/2D h-BN/GCE	Nitrite ion	River water	Providing a high surface area and increasing catalytic activity of Cu NPs	0.09–9853.45 μM	0.03 μM	70
Nafion/Mb[h)]/2D h-BN/CILE[i)]	TCA[j)]	Tap water	Good biological compatibility and high specific surface area, accelerated electron transfer rate of Mb	0.2 ∼ 30 mM	0.05 mM	92
L-cysteine/Triazine/2D h-BN/GCE	Cu^{2+} ions	Aqueous solutions	Proving good compatibility and high surface area for amino and sulfur functional groups	Not mentioned	Not mentioned	51
Defect rich 2D h-BN/GCE	4-AP[k)] and Ph[l)]	Tap and lake water	Providing a high surface area with high accessible active sites and fast electron transfer due to detective structure	0.01–30 μM (4-AP), 0.1–30 μM (Ph)	0.003 (4-AP), 0.035 (Ph) μM	76
Au NPs/2D h-BN/GCE	Hydrogen peroxide	Not mentioned	Providing a high surface area to enhance the loading amount of H_2O_2	0.04–50 mM	8.3 μM	45
Au NPs/2D h-BN/GCE	Luteolin	Peanut hulls and Perilla	Providing a high surface area for loading Au NPs and increasing their catalytic activity	10–400 pM and 0.02–10 μM	1.7 pM	59
MIP/Au NPs/2D h-BN/GCE	DES[m)]	Urine samples	Providing a high surface area for loading Au NPs and increased their catalytic activity	5 pM—0.02 μM	0.1 pM	47
Au NPs/2D h-BN/FTO[n)]	Mb	Blood serum	Providing a high surface area and increased catalytic activity of Au NPs	0.1–100 μg ml^{-1}	34.6 ng ml^{-1}	61
MIP/Fe@Au NPs/2D h-BN/GCE	CYP[o)]	Wastewater	Providing a high surface area for hosting Fe@Au NPs	10^{-13}–10^{-8} M	0.03 pM	50
Au@Pd NPs/2D h-BN	Bacillus anthracis	Culture broth	Providing a high surface area for loading Au@Pd NPs as well as hosting Ab$_2$ antibodies	5 pg ml^{-1} to 100 ng ml^{-1}	1.0 pg ml^{-1}	93
HMICl[p]-Pt NPs/POM[q)]/2D h-BN/POMBNS/CPE[r)]	N-hydroxysuccinimide	Drinking, river, and well water samples	Providing a high surface area for hosting Pt NPs	0.1–300 μM	60 nM	94
MIP/GQDs/2D h-BN/GCE	SER[s)]	Urine samples	Providing a high surface area and acceleration of charge transfer	0.001–10 nM	0.2 pM	48
		Urine samples		0.001–10 nM	0.1 pM	49

Table I. (Continued).

Modified Electrode	Analyte (s)	Detection Environment	Role of 2D h-BN	Linear Range	LOD	References
f-MWCNTs[t]/2D h-BN/ GCE	β-Agonists (RAC[u], PEA[v], SAL[w], and CLE[x])		Providing a high surface area for catching analytes and increasing the catalytic property of f-MWCNTs			
2D h-BCN/carbon cloth	DA and UA[y]	Not mentioned	Ability to alloy with carbon with minimal internal stress due to its almost similar bond length (1.7%) with C-C bond	10–300 μM (DA), 10–500 μM (UA)	5 μM (DA), 2 μM (UA)	77
2D h-BN/Si	Methane	—	Providing high surface area and exposure all of its B and N atoms to gas molecules	—	—	67
Pt NPs/2D h-BN aero-gels	Propane	—	Providing high surface area and high thermal conductivity for heat dissipation	—	—	75

a) Boron nitride quantum dot. b) Gold screen-printed electrode. c) Molecule imprinted polymer. d) Glassy carbon electrode. e) Graphene oxide. f) Dopamine. g) Nanoparticles. h) Myoglobin. i) Ionic liquid modified carbon paste electrode. j) Trichloroacetic acid. k) 4-aminophenol. l) Phenol. m) Diethylstilbestrol. n) Fluorine-doped tin oxide. o) Cypermethrin. p) 1-hexyl-3-methylimidazolium chloride. q) Polyoxometalate. r) Carbon Paste Electrode. s) Serotonin. t) Functionalized multi-walled carbon nanotubes. u) Ractopamine. v) Phenylethanolamine A. w) Salbutamol. x) Clenbuterol. y) Uric Acid.
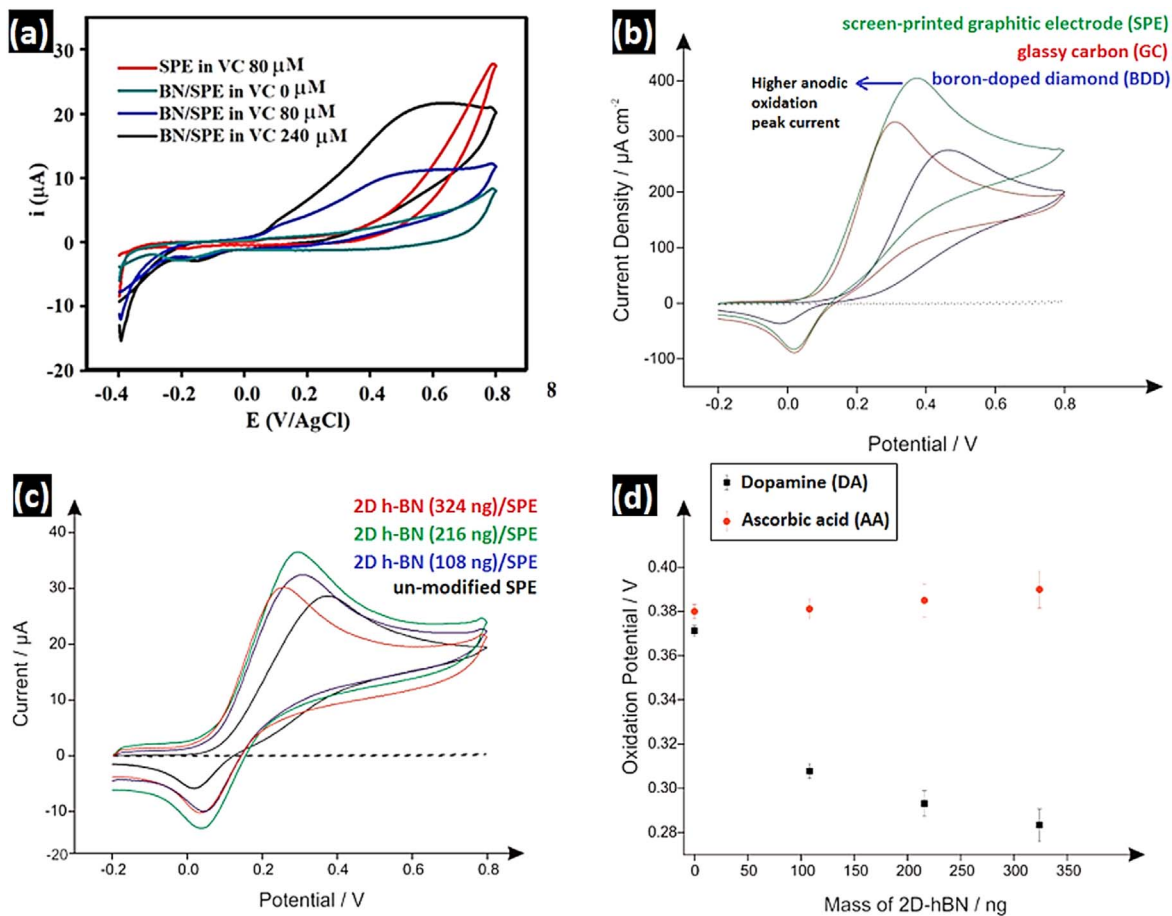
Figure 5. (a) CV plots of functionalized and un-functionalized GSPE electrodes at various concentrations of vitamin C (scan rate = 10 mV s^{-1}) (Reprinted with permission from American Chemical Society, Copyrights 2018).[65] Comparative CV curves of (b) SPE, GC, and BDD substrates and (c) 2D h-BN-modified SPE electrode and bare SPE electrode in electrocatalytic sensing of DA at the scan rate of 100 mV s^{-1}; (d) potential difference in simultaneous detection of DA and AA by 2D h-BN/SPE electrode (Reprinted with permission from American Chemical Society, Copyrights 2016).[23]

rich h-BN/GCE electrochemical sensor for these target substances in tap and lake water. Ph and 4-AP are extensively used in a variety of products and their over-absorption can cause severe health problems.[101,102] Thus, their accurate measurements are one of the main priorities of health and environmental organizations. According to the electrocatalytic response by CV examinations (Fig. 7a), the defect-rich h-BN/GCE electrode displayed higher anodic current peaks as a result of simultaneous oxidation of 4-AP and Ph compared to bare GCE electrode. This observation indicated the ameliorated catalytic activity of h-BN-modified GCE electrode with low values of LOD (0.003 and 0.035 μM for 4-AP and Ph, respectively) which originates from fast electron transfer as a result of its defect-rich structure and abundant catalytic active sites. In addition, the distinctive potential gap (603 mV) between correspondence oxidation voltages of present analytes (0.822 V for Ph and 0.219 V for 4-AP) in Fig. 7b clearly confirmed their simultaneous detection. According to literature,[42,86] structural defects (like vacancy, Stone-Wales, impurities, edges, and grain boundaries) are inseparable parts of 2D h-BN synthesis and are fortunately very effective in manipulating h-BN's large band gap for electronic applications. A schematic illustration of the electrochemical sensing mechanism of the electrode is depicted in Fig. 7c.

Moreover, due to high surface area of 2D h-BN and subjecting all of its B and N atoms to catching target gas molecules, it is an interesting material in gas sensing industry as it can expose all of its B and N atoms for catching target gas molecules. For this purpose, highly-crystalline few-layered 2D h-BN sheets were deposited on a silicon substrate via CO_2-pulsed laser to study their catalytic sensing against methane gas (CH_4).[67] Then, a simple gas sensor device was constructed in which the as-synthesized 2D h-BN sheets/Si was connected to a battery and a resistor to form a current-voltage-resistor (I-V-R) circuit.

The gas sensing response of 2D h-BN/Si sensor induced a voltage drop in the resistor; therefore, the fluctuations of the electrical conductivity at the surface could be measured. In general, the electronic property of a gas sensing material can dramatically change as a result of adsorbing and interaction with gas molecules, which is the essence of catalytic gas sensing. For corresponding 2D h-BN sheets, the polarized CH_4 molecules can easily get absorbed by the B and N atoms and turned it into a good resistor against CH_4. As Figs. 7d shows, the gas response of the 2D h-BN /Si sensor was recorded by measuring the electrical resistance of its surface in eight cycles when the CH_4 gas was pumped "in" and "out" of the chamber. Prior to exposing the 2D h-BN /Si sensor to CH_4, the electrons can freely move across the grain boundaries of the crystalline 2D h-BN, therefore the electrical resistance is at lowest value. But, as soon as the CH_4 gas was pumped into the chamber, the high surface area of 2D h-BN sheets adsorbed these polarized molecules quickly. Upon adsorption of CH_4 molecules to h-BN grain boundaries, free electrons are evacuated from those regions and a potential barrier is generated which ultimately turned the tested sensor to a good resistor against CH_4. Fast response, good repeatability, and quick recovery time was deduced from Figs. 7d, confirming the great gas sensing potential of 2D h-BN/Si electrodes.[67]

Functionalized 2D h-BN nanocomposites used for electrochemical sensors.—2D h-BN can be used as an excellent component of
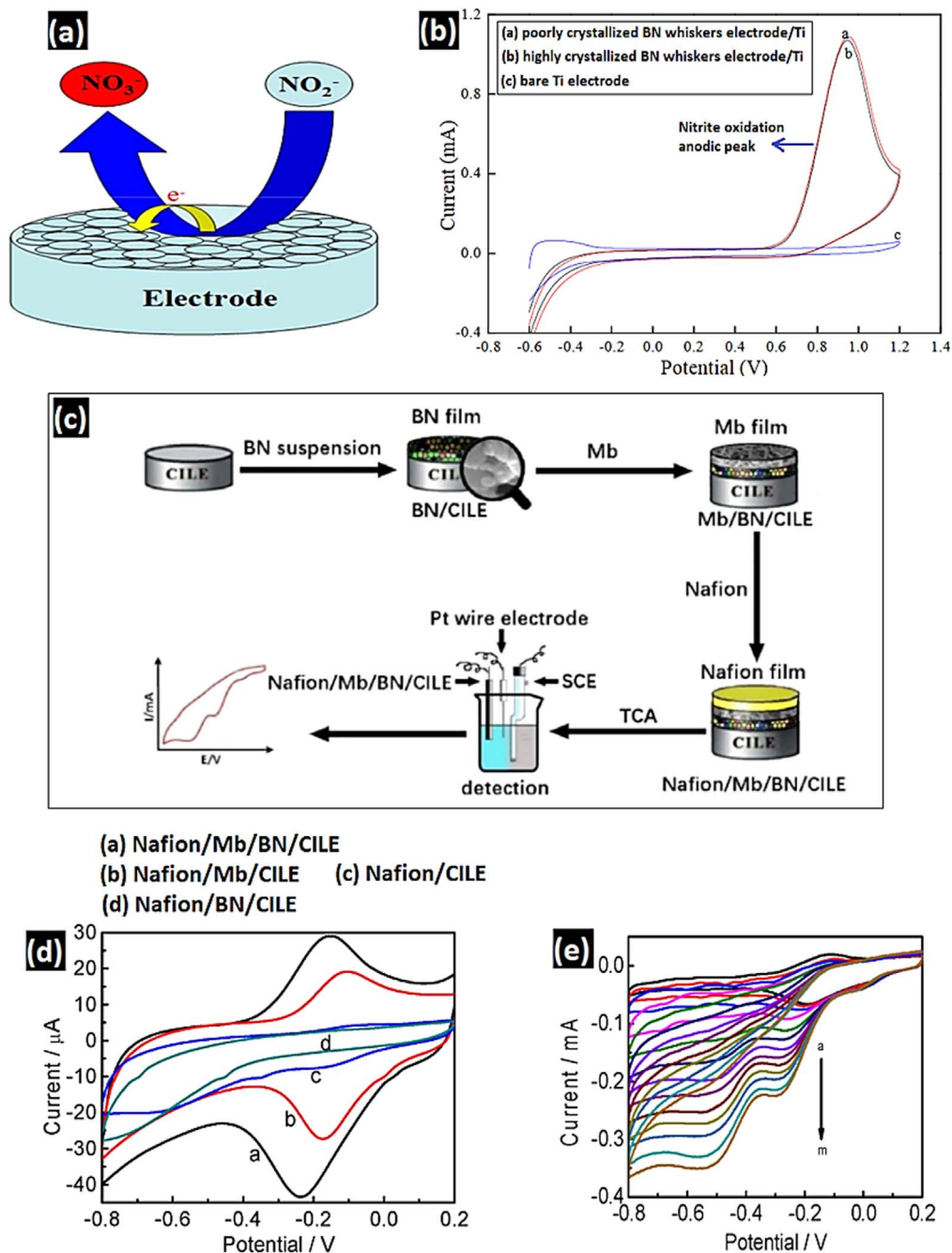
Figure 6. (a) Schematic illustration of electrochemical nitrite sensing of h-BN whiskers in water samples, (b) comparative CV curves of modified and unmodified Ti electrodes in nitrite detection (Reprinted with permission from the Royal Society of Chemistry, Copyrights 2016).[69] (c) Schematic illustration of Nafion/Mb/h-BN/CILE electrochemical sensor for TCA detection, (d) comparative CV analysis of modified and un-modified CILE electrodes at the scan rate of 100 mV s^{-1}, (e) CV curves of Nafion/Mb/h-BN/CILE electrode in electrocatalytic sensing of TCA with various concentrations (from 0.2 to 30 mM) (Reprinted with permission from WILEY-VCH, Copyrights 2018).[92]

nanocomposites based electrochemical sensors. In a recent study,[45] the electrochemical behavior of 2D h-BN functionalized with Au NPs on GCE toward hydrogen peroxide (H_2O_2) detection was examined. The CV analysis revealed high electrocatalytic sensing of Au NPs/BN/GCE electrode in the presence of H_2O_2 through appearance of high intensity catalytic peak at −0.53 V, shown in Fig. 8a. This dramatic improvement of the catalytic activity with an LOD of 8.3 μM is due to the synergistic effect of Au NPs and 2D h-BN sheets. The former offers good electrocatalytic activity toward H_2O_2 sensing and the latter supplies high specific surface area to lodge high amounts of H_2O_2. The electrochemical interaction of H_2O_2 on the surface of Au NPs/2D h-BN hybridized nanostructures

is suggested as follows: first, H_2O_2 interacts with Au NPs to produce gold hydroxide (Eq. 12).

$$2Au(s) + 3H_2O_2(aq) \rightarrow 2Au(OH)_3(aq) \qquad [12]$$

Then, the gold hydroxide is reduced to its initial Au metallic form (Eq. 13).[105]

$$Au(OH)_3(aq) + 3e^- + 3H^+(aq) \rightarrow Au(s) + 3H_2O(aq) \qquad [13]$$
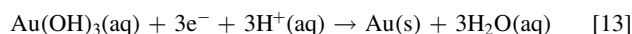
The electronic state of Au NP/h-BN nanostructures changes and facilitates charge transfer at the interface as a result of hybridization (Fig. 8b).[103,106] When Au NPs attach to the surface of 2D h-BN
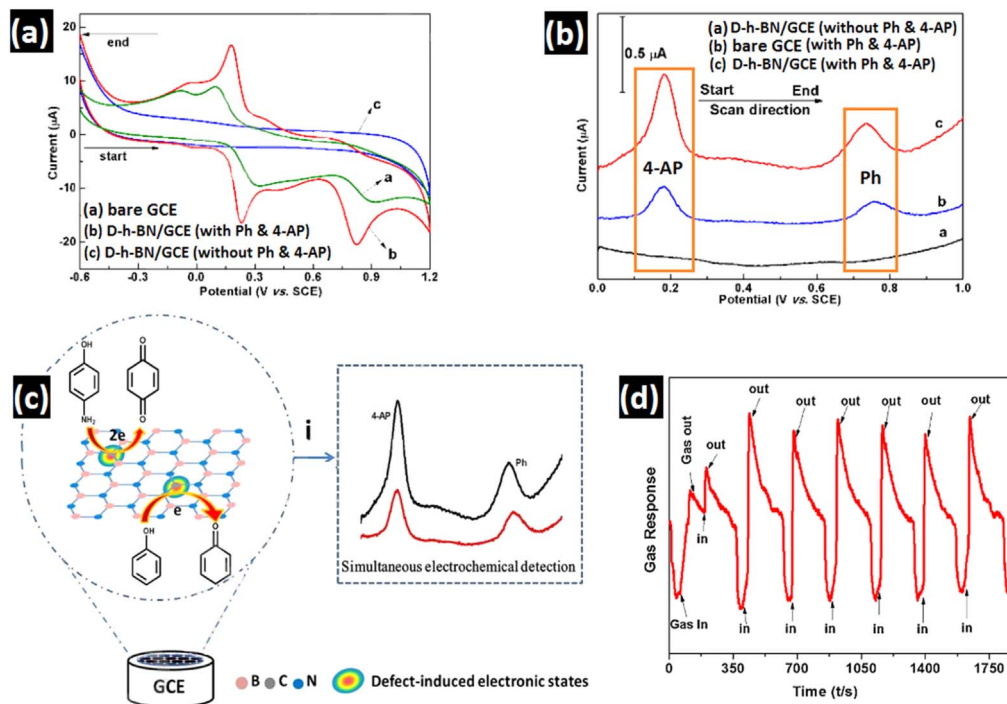
Figure 7. (a) CV graphs of defect-rich-based electrodes in 0.2 M sodium acetate and acetic acid buffer solution at the scan rate of 100 mV s^{-1}, (b) DPV profiles of electrodes in the simultaneous presence/absence of 4-AP and Ph analyts; (c) schematic illustration of defect-rich 2D h-BN electrochemical sensing for simultaneous detection of 4-AP and Ph (Reprinted with permission from Elsevier, Copyrights 2019).[76] (d) Gas response (electrical resistance) curve of highly crystalline 2D h-BN sheets/Si sensor against CH$_4$ (Reprinted with permission from Elsevier, Copyrights 2014).[67]

sheets, surface plasmons are produced at their interface and consequently induce local electric fields. These plasmonic local fields can reduce the 2D h-BN band gap via charge redistributing compared to pure h-BN.[86,103,107,108] Moreover, Fig. 8b in terms of band structure clearly demonstrates that combining Au NPs and 2D h-BN in a nanocomposite ultimately leads to rearrangement of the band structure, equalizing their Fermi levels and reducing the band gap due to mixing of Au NPs-5d orbitals and N-p$_z$ orbitals of 2D h-BN. As already discussed, when 2D h-BN is modified by a conductive support material like metal NPs (Au, Pt, etc.), the N-p$_z$ and B-p$_z$ orbitals in 2D h-BN interact with the d$_z^2$ metal orbitals which can intensify the electrocatalytic activity of such hybrid structures.[6,86,97,98]

Fu et al.[59] also took advantage of the excellent electrocatalytic sensing characteristics of the Au NPs/2D h-BN/GCE nanocomposite for detection of redox active luteolin (C$_{15}$H$_{10}$O$_6$) in peanut hulls and Perilla. Luteolin as an important nature-based flavonoid has a variety of pharmacological benefits. Therefore, its accurate and cost-effective detection in plants and pharmaceutical samples by electrochemical sensing is crucial. Prior to detection of luteolin, the electrochemical performance of fabricated Au NPs/2D h-BN/GCE electrode was examined by CV technique. The obtained results demonstrated the higher current responses of [Fe(CN)$_6$]$^{3-/4-}$ redox peaks and more expanded integrated area under CV curve for the hybrid electrode compared to unmodified ones (Fig. 8c), indicating an enhanced electrochemical performance. In Fig. 8d, evaluation of catalytic activity shows that the electrode exposed to luteolin possessed the highest oxidation peak output current compared to 2D h-BN/GCE and bare GCE electrodes, which is originated from both high surface area of 2D h-BN and catalytic activity of Au NPs. This provides an LOD as low as 1.7 pM. A schematic illustration of the electrochemical redox mechanism of luteolin is shown in the inset of Fig. 8d.[104]

Recently, amine functionalized 2D h-BN loaded by Fe@Au NPs core-shell structure was utilized to fabricate Cypermethrin (CYP, C$_{22}$H$_{19}$Cl$_2$NO$_3$) molecular imprinted polymer (MIP) sensors for

wastewater samples.[50] CYP is a common pesticide with high stability in the environment; thus, either short-term or long-term exposure to it may render serious health issues. Thereby, precise and continuous detection of CYP is crucial. As seen in Fig. 8e, output current of generated [Fe(CN)$_6$]$^{3-/4-}$ redox peaks for Fe@Au NPs/ 2D h-BN/GCE nanocomposite electrode has increased while peak potential difference (ΔE_P) has decreased compared to un-functionalized electrodes. Therefore, an improvement in electrochemical performance due to this collaborative cooperation can be achieved. In addition, facilitated charge transportation and reduced mass transfer resistance due to the reduced band gap of 2D h-BN is the reason behind the small reported LOD (0.03 pM) and improved electrocatalytic sensing property against CYP (Fig. 8f).

Likewise the previous research, a novel immunosensor based on bimetallic palladium (Pd)-gold NPs functionalized 2D h-BN nanocomposite was proposed in 2016.[93] Significance of Bacillus anthracis detection, as a bacterium and a serious biological weapon, is ever-increasing, particularly in agriculture-based countries.[109,110] The formation of Au@Pd NPs/2D h-BN nanocomposite is based on Lewis acid-base interaction between 2D h-BN sheets as Lewis acid and Au@Pd NPs as Lewis base. The electron deficient 2D h-BN sheets with their intrinsic high surface area can absorb target analytes efficiently and enhance the catalytic activity of conductive Au@Pd NPs. This was evaluated through the reduction of 4-nitrophenol (4-NP, C$_6$H$_5$NO$_3$) to 4-aminophenol (4-AP, C$_6$H$_7$NO) using UV-visible spectroscopy analysis. Upon introduction of Au@Pd NPs/h-2D catalyst in the presence of NaBH$_4$, a new absorption peak appeared at 300 nm within 20 s, which was an indicator of swift, successful catalytic reduction of 4-NP to 4-AP. In addition, gas chromatography-mass spectrometry analysis confirmed that the fast-catalytic reduction of 4-NP is completed in less than 3 min (Fig. 9a). The electrochemical immunosensing of Au@Pd NPs/2D h-BN electrode was examined using CV analysis. For this purpose, Au@Pd NPs/2D h-BN was conjugated with mouse α-B. anthracis surface array protein (SAP) antibodies (Ab$_2$) referred as Au@Pd NPs/2D h-BN/Ab$_2$ bionanolabel and was connected to
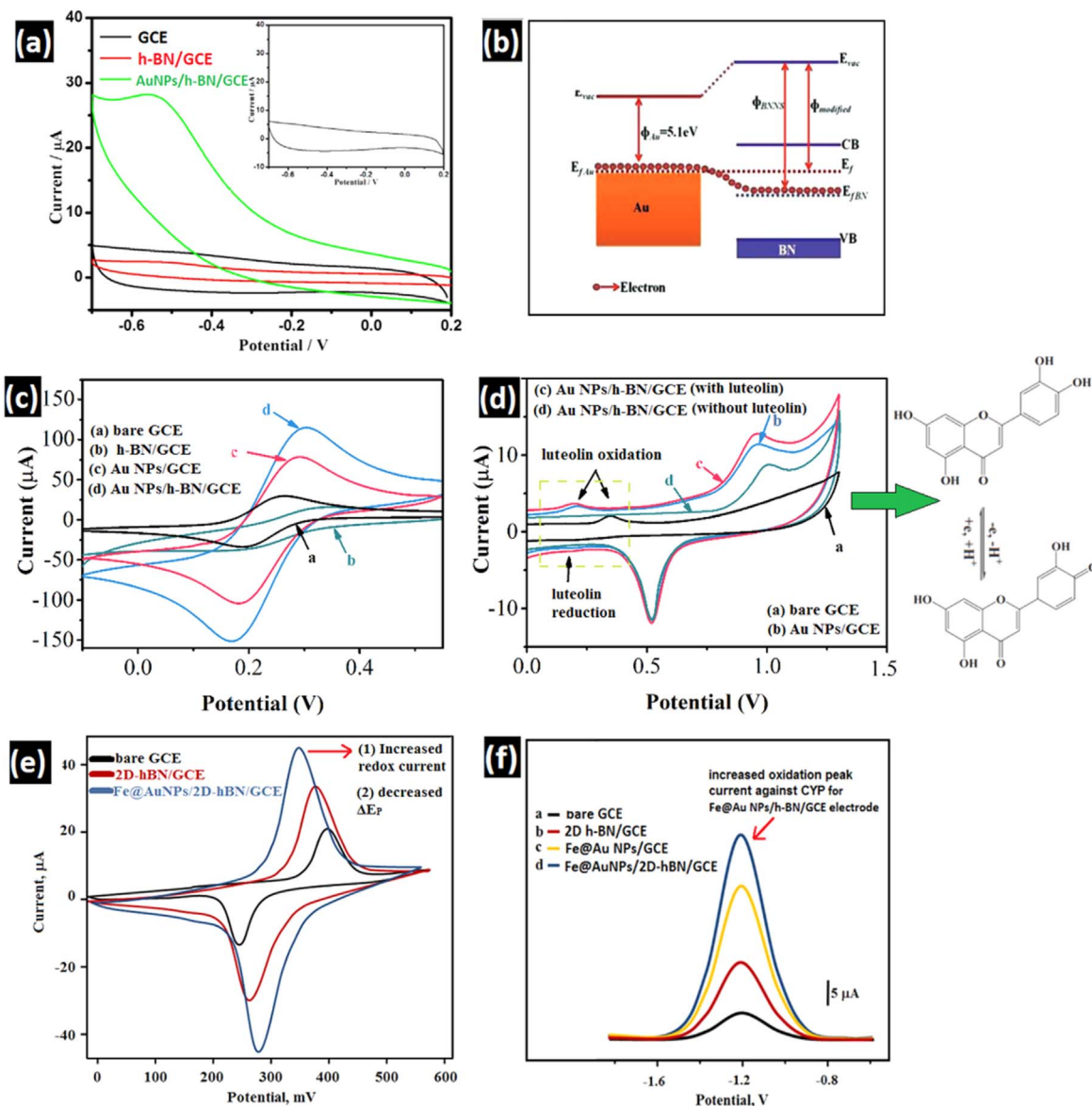
Figure 8. (a) Comparative CV curves of bare GCE, 2D h-BN/GCE, and Au NPs/2D h-BN/GCE electrodes in the presence of 10 mM H_2O_2 at the scan rate of 50 mV s^{-1} (inset: CV curve of Au NPs/2D h-BN/GCE electrode in the absence of H_2O_2) (Reprinted with permissions from Elsevier, Copyrights 2014).[45] (b) Schematic illustration of energy band of Au NPs-loaded 2D h-BN sheets (Reprinted with permission from WILEY-VCH, Copyrights 2013).[103] (c) Comparative CV profiles of modified and un-modified GCE electrodes in the presence of 5 mM $[Fe(CN)_6]^{3-/4-}$ as redox probe; (d) electrocatalytic sensing CV curves of modified and un-modified GCE in the presence and absence of 0.1 μM luteolin (scan rate=50 mV s^{-1}) (Reprinted with permissions from Elsevier, Copyrights 2018),[59] inset: Electrochemical reaction mechanism of luteolin (Reprinted with permissions from ESG, Copyrights 2017).[104] (e) Comparative CV curves functionalized and un-functionalized GCE electrodes in the presence of 1 mM $[Fe(CN)_6]^{3-/4-}$. as redox probe at the scan rate of 200 mV s^{-1}; (f) Differential pulse voltammetric (DPV) of all the molecular imprinted electrodes after rebinding of 10 nM CYP (Reprinted with permission from IOP Publishing Ltd., Copyrights 2018).[50]

Cobalt (II) phthalocyanine (CoPC)/Chitosan (CS)/Rabbit α-B. anthracis Sap antibodies(Ab$_1$)/ B. anthracisSap antigen/GCE electrode to build a complete immunosensor, as illustrated in Fig. 9c. Finally, the catalytic reduction of 4-NP to 4-AP in the bionanolabel appeared with higher anodic peak current than the unmodified bionanolabels, as shown in Fig. 9b. The exceptional immunosensing activity of the electrode with a small LOD (1.0 pg ml^{-1}) was fast and was not disturbed after conjugation with Ab$_2$ owing to the high accessible surface area of 2D h-BN sheets that not only lodged bimetallic Au-Pd NPs, but also hosted Ab$_2$ antibodies. The schematic representation of the sensor and its electrochemical mechanism is shown in Fig. 9c.[93]

Alternatively, 2D h-BN functionalized with sulfur-modified graphene quantum dots (S-GQDs) has been shown to be capable of Serotonin (SER, $C_{10}H_{12}N_2O$) detection. The sensor is fabricated by drop casting of the electroactive material on a GCE, then the SER-containing phenol (MIP) was applied on the GQDs/2D h-BN/GCE electrode.[48] Firstly, the electrochemical performance assessment of the electrode by CV technique exhibited an increment in $[Fe(CN)_6]^{3-/4-}$ redox current peaks and also reduction of ΔE_P (30 mV) compared to the other electrodes (Fig. 9d). This improved electrochemical performance was attributed to facilitated charge transport that arises from reduced band gap of h-BN due to hybridization with GQDs.

According to literature,[6,86] interaction of h-BN nanomaterials with graphene (or hexagonal graphitic structure) may result in the formation of a complex ternary system, so-called boron carbonitride $B_xC_yN_z$. These hybridized structures are made by embedding graphene to h-BN or vice versa. Theoretical studies have revealed that the band gap of h-BN (5.7 eV) decreases by carbon
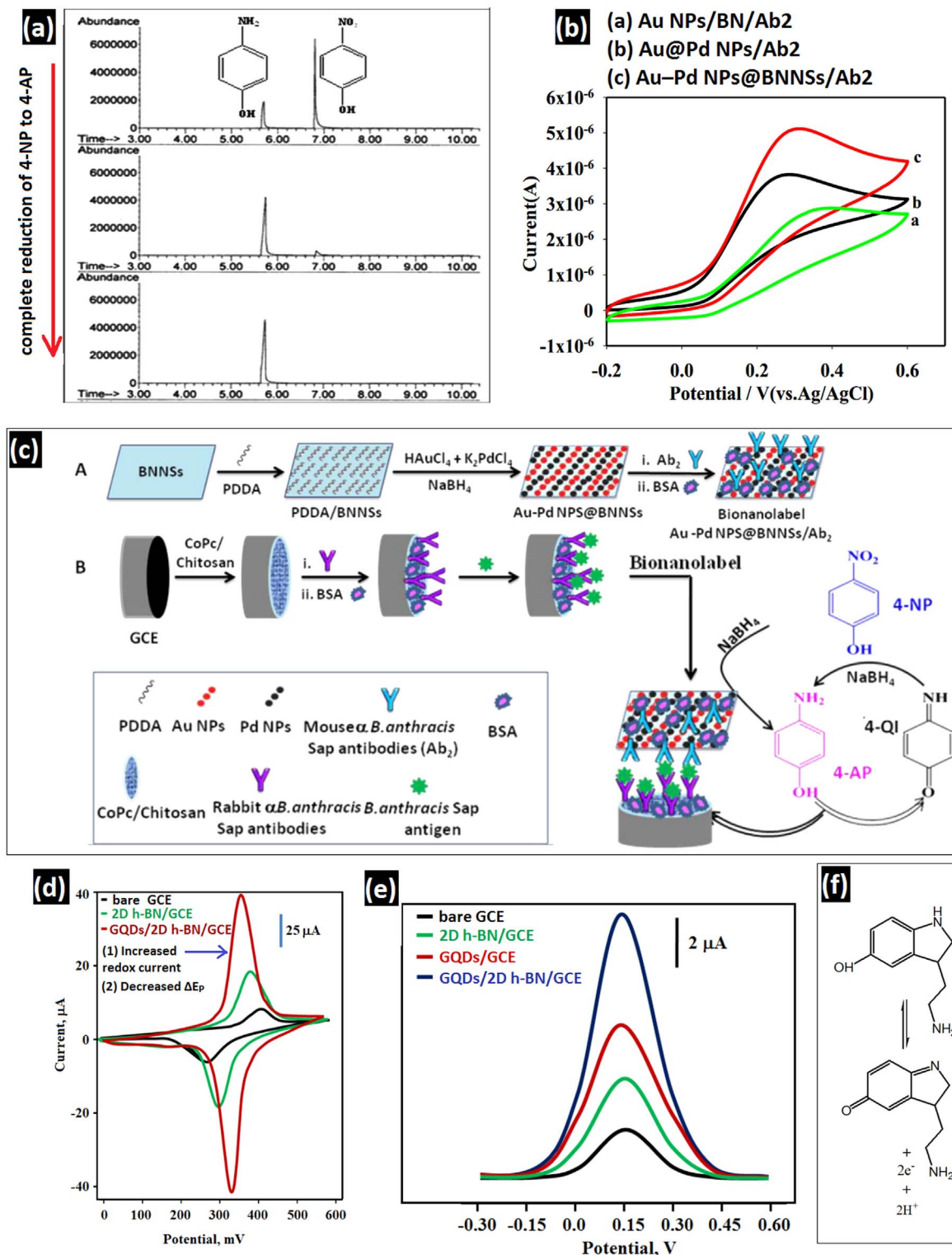
Figure 9. (a) GC–MS chromatograms spectrum of complete catalytic reduction of 4-NP to 4-AP by Au@Pd NPs/2D h-BN nanocomposite; (b) CV measurements for immunosensing using various bionanolabels based on Au NPs, 2D h-BN conjugated with α-B. anthracis SAP antibodies (Ab₂); (c) schematic illustration of (A) Au@Pd NPs/2D h-BN /Ab₂ bionanolable synthesis and (B) correspondence electrochemical immunosensor and its catalytic mechanism (Reprinted with permission from Elsevier, Copyrights 2016).[93] (d) Comparative CV curves of functionalized and un-functionalized electrodes based on GQDs and/or 2D h-BN in the presence of 1 mM $[Fe(CN)_6]^{3-/4-}$ as redox probe at the scan rate of 200 mV s⁻¹; (e) DPV of various molecular imprinted electrodes after rebinding of 1 nM SER as analyte, (f) electrochemical oxidation mechanism of SER at the surface of MIP/GQDs/2D h-BN/GCE electrode (Reprinted with permission from Elsevier, Copyrights 2018).[48]

concentration (e.g. 1 eV for 24% C), indicating escalated electron transport in carbon-doped h-BN as compared to pure h-BN. Figure 9e represents the differential pulse voltammetry (DPV)

analysis of MIP/GQDs/2D h-BN/GCE electrode, endorsing the emergence of an SER oxidation peak and efficient electrocatalytic sensing activity of electrode against SER in urine samples with an
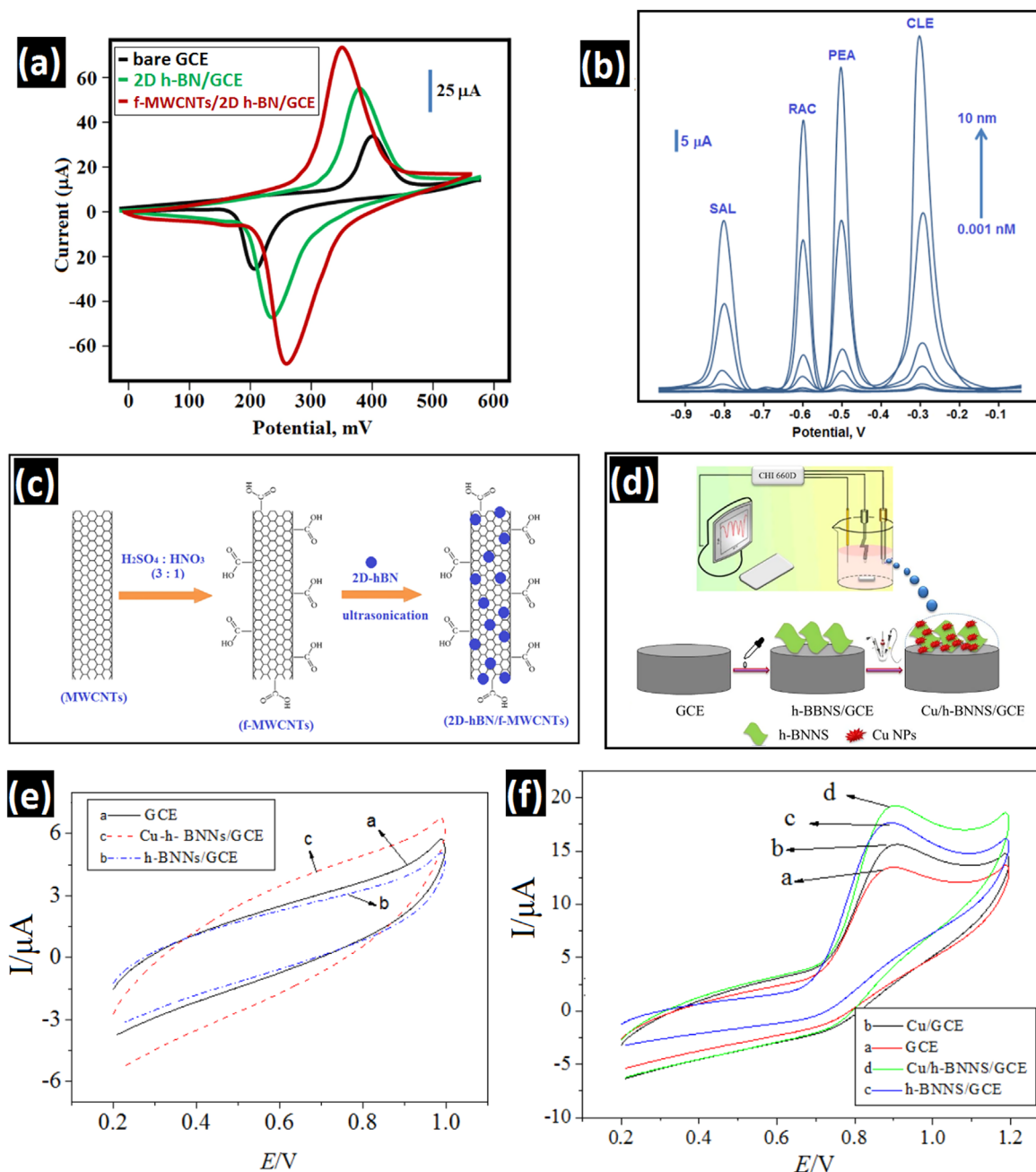
Figure 10. (a) Comparative CV plots of functionalized and un-functionalized f-MWCNTs and/or 2D h-BN-functionalized GCE electrodes in the presence of 1 mM $[Fe(CN)_6]^{3-/4-}$ as redox probe at the scan rate of 200 mV s^{-1}; (b) DPV profiles of f-MWCNTs/2D h-BN/GCE electrode in with various PEA, CLE, RAC, and SAL concentrations (from blank to 10 nm of analytes); (c) schematic illustration of f-MWCNTs/2D h-BN hybrid electrode (Reprinted with permission from Elsevier, Copyrights 2019).[49] (d) schematic preparation demonstration Cu NPs/2D h-BN /GCE sensor; CV profiles of Cu NPs and/or 2D h-BN-functionalized GCE electrodes in the (e) 1 mM $[Fe(CN)_6]^{3-/4-}$ as redox probe and (f) 2 mM NO$_2^-$ as analyte (scan rate = 100 mV s^{-1}) (Reprinted with permission from ESG, Copyrights 2018).[70]

LOD as small as 0.2 pM compared to bare electrodes. The mechanism of this electrochemical oxidation of SER at the surface of hybridized electrode is depicted in Fig. 9f. This surface modification of h-BN with carbon nanomaterials have also been studied for an ultra-sensitive electrochemical sensor for simultaneous determination of β-Agonists such as ractopamine (RAC), phenylethanolamine A (PEA), salbutamol (SAL), and clenbuterol (CLE) in urine samples through hybridization of functionalized multi-walled carbon nanotubes (f-MWCNTs) and 2D h-BN sheets.[49] The mentioned β-Agonists compounds are illegally used in some food products and can cause severe food poisoning. Thus, they require immediate and fast detection. According to the obtained

results, the electrochemical performance of f-MWCNTs/2D h-BN/ GCE electrode exceeded the un-modified ones by showing increased redox peak currents, enlarged integrated area, and decreased ΔE$_P$ (Fig. 10a). Surprisingly, it revealed superb electrocatalytic response towards simultaneous determination of RAC, PEA, SAL, and CLE by a distinctive voltage gap among their individual oxidation peaks (Fig. 10b). This enhanced electroanalytical activity of f-MWCNTs/ 2D h-BN/GCE electrode is arisen from Lewis acid-base interaction of 2D h-BN sheets (Lewis acid) and f-MWCNTs (Lewis base). F-MWCNTs has unbounded electron pairs in its –COOH functional groups which can provide fast and efficient electron transportation; 2D h-BN sheets possess high specific surface area for catching target
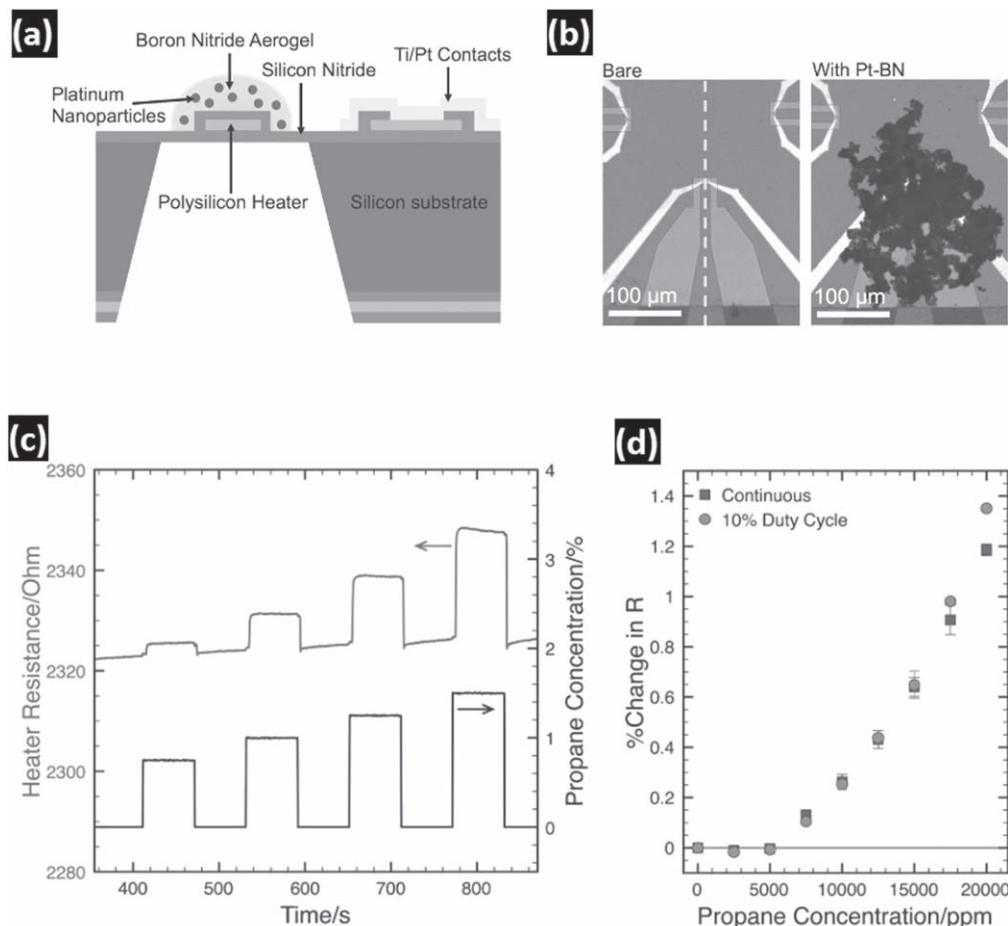
Figure 11. (a) Schematic illustration of Pt NPs/2D h-BN aerogels-containing microheater; (b) optical images of the microheater before and after Pt NPs/2D h-BN deposition; (c) gas response of the sensor during exposure to various propane concentrations; (d) catalytic response of sensor to continuous heating of propane to 500 °C and for 100 ms every second which lead to reduced required power to 1.5 mW (Reprinted with permission from WILEY-VCH, Copyrights 2016).[75]

substances which can improve the catalytic capacity of f-MWCNTs (Fig. 10c). Thereby, merging these two superior materials caused facilitated charge transfer and reduction of resistance that ultimately led to an improved electrochemical sensing property with a low reported LOD of 0.1 pM.[49]

In another work, Zhang et al.[70] took advantage of the efficient interaction between metal NPs (Cu in particular) and 2D h-BN sheets in altering the electronic states of boron nitride toward improving the catalytic activity in NO_2^- determination. Nitrite as a carcinogenic agent is extensively used in human-related environments and industry, and its omnipresence in our lives is inevitable. However, large amounts of nitrite in human body can reduce the oxygen transport, therefore their detection is vital in biological samples. The underlying mechanism of nitrite's electrochemical detection lies in its redox mechanism according to Eq. 14:

$$NO_2^-(aq) + H_2O(aq) + 2e^-(aq) \rightarrow NO_3^-(aq) + 2H^+(aq) \quad [14]$$
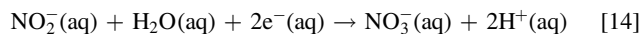
For this purpose, Cu NPs/2D h-BN nanocomposite was drop cast on a GCE electrode as shown in Fig. 10d and its catalytic response was assessed in river water samples. The obtained results from CV technique (Fig. 10e) endorsed its superior electrochemical performance through revealing the more expanded integrated area and higher output current that stemmed from coupling of 2D h-BN and conductive Cu NPs. Increased output current response in the presence of NO_2^- at ~0.9 V giving an LOD of 0.03 μM (Fig. 10f). The improved catalytic behavior arises from reduced band gap of BN as a result of hybridization with Cu NPs.

As mentioned earlier, 2D h-BN surface and its active edges are providing an excellent platform for gas sensing. Recently, a Pt NP-decorated 2D h-BN aerogel hybrid (Pt NPs/2D h-BN aerogel) was developed for swift and low-powered propane gas (C_3H_8) sensing.[75] The low-power gas sensors are receiving tremendous attention due to their efficient leak detection of combustible gases. Prior any analysis, the catalytic gas sensor was prepared by drop casting Pt NPs/2D h-BN aerogel onto a low-power microheater (500 °C). The schematic illustration of the cross section and optical images of a catalytic gas sensor prepared by drop casting of Pt NPs/2D h-BN aerogel onto a low-power microheater are shown in Figs. 11a and 11b, respectively. The gas sensing response of Pt NPs/2D h-BN-integrated microheater sensor was measured by $\frac{R - R_0}{R_0} \times 100\%$, where R_0 and R are the average resistances in air and during exposure to specific concentration of C_3H_8, respectively.

Since the polysilicon microheater has a positive thermal coefficient resistance (TCR), the resistance is at the lowest state prior to infusion of propane to the chamber. However, as soon as the propane gas is purged into the sensor, the exothermic reaction with oxygen molecules (combustion) on the surface of Pt NPs generates heat. Owing to the high thermal conductivity and high surface area of 2D h-BN, the generated heat is efficiently transferred to the polysilicon microheater and increases its temperature and electrical resistance (due to the positive TCR). Using the sensor resistance in air of (R_0) and in a wide range of propane concentrations (R), the full sensor response over time can be calculated by the above equation. It only took 1.35 s for the sensor to reach 90% of its full potential (Fig. 11c) which is significantly better than commercial sensors with response

time of 10−20 s. Moreover, quick response and recovery time (<2 s) through various concentrations of propane confirmed the highly sensitive catalytic gas sensing of Pt NPs/2D h-BN sensors. Eventually, both continuous and stepped heating of propane reduced the required power to 1.5 mW (Fig. 11d), which is 2 orders of magnitude less than commercially available gas sensors. The superior property of this novel hybrid undoubtedly paves the way for wireless, low-power catalytic gas sensors.[75] Table I provides a comprehensive summary of all reported electrochemical sensors based on 2D h-BN.

Conclusions

To recapitulate, two-dimensional boron nitride nanomaterials and nanocomposites have revealed appealing electrochemical characteristics due to their large specific surface area, porous structure, N- and B-active edges, chemical and thermal stability, structural defects, and dominant catalytic behavior. Moreover, their electronic band structure and HOMO-LUMO gap can be tuned via interaction with other nanomaterials in the form of heterostructures or chemical functionalization. However, their electrically insulating restrictions as well as potential charge trapping over the films due to structural defects have traditionally suppressed their great potential as an ideal electrochemical platform. To address this challenge, 2D h-BN nanostructures have been hybridized with different metal nanoparticles (such as gold, platinum, and copper) to acquire synergistic effect from the abundant catalytic sites and high electrical conductivity of these constituents, respectively. Moreover, there have been efforts to tune the band gap of BN through grafting functional groups (e.g. hydroxyl, amine, and fluorine), doping of external atoms (e.g. oxygen and carbon), and even interaction with the electrode surface. This occurs through symmetry disruption of the HOMO-LUMO gap and inducing the mid-energy levels to above or below the Fermi level. The defectivity of 2D h-BN also increases its active catalytic sides and reduces the band gap, providing a fertile substrate for electrochemical reactions. Therefore, when modified 2D h-BN based electrodes are exposed to different analytes, signal intensity increases, overpotential difference is often reduced, and a nM–pM sensitivity can be obtained in such electrochemical sensors.

However, despite a great deal of attention and recent studies on electrochemical sensing using 2D h-BN sheets, this research topic is still in its infancy. The first step is to develop simple, low-cost, and high-yield synthesis and exfoliation methods to produce 2D h-BN. Controlling the lateral size, number of layers, and functional groups in 2D h-BN is crucial as all these parameters affect the material's performance as a sensing platform. In the next step, the effect of surface interactions, dopant concentration, and structural defect types on sensor performance are to be explored to enable examining new sensing applications of 2D h-BN. Additionally, hybridizing 2D h-BN with small band-gap 2D materials such as MoS_2 or WS_2, which also have catalytic properties, can be a new approach towards novel sensors. Although 2D h-BN sheets have been used as a new sensor platform successfully in recent years, many more potential applications of BN-based sensor platforms in various sensing fields can be envisaged in the near future. Finally, it is important to examine the performance of 2D h-BN sensors as compared with other 2D nanomaterial-based sensors examined in the same condition to explore the benefits and shortcomings of the 2D material-based sensors for practical applications.

Acknowledgments

ORCID

Shayan Angizi https://orcid.org/0000-0002-5345-4271
Sayed Ali Ahmad Alem https://orcid.org/0000-0003-0539-9332
Amir Pakdel https://orcid.org/0000-0001-5852-0808
Amir Hatamie https://orcid.org/0000-0002-7085-893X

References

1. A. Hatamie, R. Rahmati, E. Rezvani, S. Angizi, and A. Simchi, *ACS Appl. Nano Mater.*, **2**, 2212 (2019).
2. E. Rezvani, A. Hatamie, M. Berahman, M. Simchi, S. Angizi, R. Rahmati, J. Kennedy, and A. Simchi, *J. Electrochem. Soc.*, **166**, H3167 (2019).
3. Y. Hu, Y. Huang, C. Tan, X. Zhang, Q. Lu, M. Sindoro, X. Huang, W. Huang, L. Wang, and H. Zhang, *Mater. Chem. Front.*, **1**, 24 (2017).
4. T. R. Kıran, N. Atar, and M. L. Yola, *J. Electrochem. Soc.*, **166**, H495 (2019).
5. A. Hatamie, S. Angizi, S. Kumar, C. M. Pandey, A. Simchi, M. Willander, and B. D. Malhotra, *J. Electrochem. Soc.*, **167**, 037546 (2020).
6. A. Pakdel, Y. Bando, and D. Golberg, *Chem. Soc. Rev.*, **43**, 934 (2014).
7. R. Jerome and A. K. Sundramoorthy, *J. Electrochem. Soc.*, **166**, B3017 (2019).
8. Y. Xue et al., *J. Mater. Chem. A*, **4**, 1469 (2016).
9. A. Pakdel, Y. Bando, and D. Golberg, *Nanotubes and Nanosheets: Functionalization and Applications of Boron Nitride and Other Nanomaterials* (CRC Press, Boca Raton, FL) p. 3 (2015).
10. D. Wickramaratne, L. Weston, and C. G. Van De Walle, *J. Phys. Chem. C*, **122**, 25524 (2018).
11. A. Hatamie, P. Jalilian, E. Rezvani, A. Kakavand, and A. Simchi, *Meas. J. Int. Meas. Confed.*, **134**, 679 (2019).
12. A. Pakdel, Y. Bando, and D. Golberg, *ACS Nano*, **8**, 10631 (2014).
13. X. Wang, A. Pakdel, J. Zhang, Q. Weng, T. Zhai, C. Zhi, D. Golberg, and Y. Bando, *Nanoscale Res. Lett.*, **7**, 662 (2012).
14. W. Sun, L. Wang, T. Wu, Y. Pan, and G. Liu, *J. Electrochem. Soc.*, **163**, C16 (2016).
15. G. Cassabois, P. Valvin, and B. Gil, *Nat. Photonics*, **10**, 262 (2016).
16. A. Hatamie, A. Echresh, B. Zargar, O. Nur, and M. Willander, *Electrochim. Acta*, **174**, 1261 (2015).
17. A. Pakdel, X. Wang, C. Zhi, Y. Bando, K. Watanabe, T. Sekiguchi, T. Nakayama, and D. Golberg, *J. Mater. Chem.*, **22**, 4818 (2012).
18. P. Bollella, G. Fusco, C. Tortolini, G. Sanzò, G. Favero, L. Gorton, and R. Antiochia, *Biosens. Bioelectron.*, **89**, 152 (2017).
19. Q. Weng, X. Wang, X. Wang, Y. Bando, and D. Golberg, *Chem. Soc. Rev.*, **45**, 3989 (2016).
20. C. Zhu, D. Du, and Y. Lin, *Biosens. Bioelectron.*, **89**, 43 (2017).
21. S. Angizi, F. Shayeganfar, M. H. Azar, and A. Simchi, *Ceram. Int.*, **46**, 978 (2020).
22. A. Razmdideh and M. T. Ahmadi, *Phys. Solid State*, **61**, 2194 (2019).
23. A. F. Khan, D. A. Brownson, E. P. Randviir, G. C. Smith, and C. E. Banks, *Anal. Chem.*, **88**, 9729 (2016).
24. J. Jiang, T. Xu, J. Lu, L. Sun, and Z. Ni, *Research*, **2019**, 1 (2019).
25. T. Sainsbury, A. Satti, P. May, Z. Wang, I. McGovern, Y. K. Gun'ko, and J. Coleman, *J. Am. Chem. Soc.*, **134**, 18758 (2012).
26. F. Shayeganfar, M. R. Rahimi Tabar, A. Simchi, and J. Beheshtian, *Phys. Rev. B*, **96**, 1 (2017).
27. H. M. Wang, Y. J. Liu, H. X. Wang, J. X. Zhao, Q. H. Cai, and X. Z. Wang, *J. Mol. Model.*, **19**, 5143 (2013).
28. E. C. Anota, A. R. Juárez, M. Castro, and H. H. Cocoletzi, *J. Mol. Model.*, **19**, 321 (2013).
29. K.-B. Kim, W. Jang, J. Y. Cho, S. B. Woo, D. H. Jeon, J. H. Ahn, S. Do Hong, H. Y. Koo, and T. H. Sung, *Nano Energy*, **54**, 91 (2018).
30. H. Xing, Q. Zhai, X. Zhang, J. Li, and E. Wang, *Anal. Chem.*, **90**, 2141 (2018).
31. Y. Bai, J. Zhang, Y. Wang, Z. Cao, L. An, B. Zhang, Y. Yu, J. Zhang, and C. Wang, *ACS Appl. Nano Mater.*, **2**, 3187 (2019).
32. Y. Xue, Q. Liu, G. He, K. Xu, L. Jiang, X. Hu, and J. Hu, *Nanoscale Res. Lett.*, **8**, 49 (2013).
33. J. Azamat, B. S. Sattary, A. Khataee, and S. W. Joo, *J. Mol. Graph. Model.*, **61**, 13 (2015).
34. W. Lei, H. Zhang, Y. Wu, B. Zhang, D. Liu, S. Qin, Z. Liu, L. Liu, Y. Ma, and Y. Chen, *Nano Energy*, **6**, 219 (2014).
35. Q. Weng et al., *Adv. Mater.*, **29**, 1 (2017).
36. X. Wei, M. Wang, Y. Bando, and D. Golberg, *ACS Nano*, **5**, 2916 (2011).
37. C. Zhao, Z. Xu, H. Wang, J. Wei, W. Wang, X. Bai, and E. Wang, *Adv. Funct. Mater.*, **24**, 5985 (2014).
38. J. Zhao and Z. Chen, *J. Phys. Chem. C*, **119**, 26348 (2015).
39. X. Liu, T. Ma, N. Pinna, and J. Zhang, *Adv. Funct. Mater.*, **27**, 1702168 (2017).
40. K. Zhang, Y. Feng, F. Wang, Z. Yang, and J. Wang, *J. Mater. Chem. C*, **5**, 11992 (2017).
41. A. Pakdel, C. Zhi, Y. Bando, T. Nakayama, and D. Golberg, *ACS Nano*, **5**, 6507 (2011).
42. Y. Lin and J. W. Connell, *Nanoscale*, **4**, 6908 (2012).
43. M. N. Ivanova, E. D. Grayfer, E. E. Plotnikova, L. S. Kibis, G. Darabdhara, P. K. Boruah, M. R. Das, and V. E. Fedorov, *ACS Appl. Mater. Interfaces*, **11**, 22102 (2019).
44. C. Zhi, Y. Bando, C. Tang, H. Kuwahara, and D. Golberg, *Adv. Mater.*, **21**, 2889 (2009).
45. G. H. Yang, A. Abulizi, and J. J. Zhu, *Ultrason. Sonochem.*, **21**, 1958 (2014).
46. X. Li, J. Shan, W. Zhang, S. Su, L. Yuwen, and L. Wang, *Small*, **13**, 1602660 (2017).
47. M. L. Yola and N. Atar, *J. Electrochem. Soc.*, **165**, H897 (2018).
48. M. L. Yola and N. Atar, *Appl. Surf. Sci.*, **458**, 648 (2018).

49. M. L. Yola and N. Atar, *Mater. Sci. Eng. C-Mater.*, **96**, 669 (2019).
50. N. Atar and M. L. Yola, *J. Electrochem. Soc.*, **165**, H255 (2018).
51. S. Daneshnia, M. Adeli, A. Yari, A. Shams, I. S. Donskyi, and W. E. S. Unger, *Mater. Res. Express*, **6**, 95076 (2019).
52. X. Zhang, Z. Lai, C. Tan, and H. Zhang, *Angew. Chemie Int. Ed. English*, **55**, 8816 (2016).
53. G. Lian, X. Zhang, M. Tan, S. Zhang, D. Cui, and Q. Wang, *J. Mater. Chem.*, **21**, 9201 (2011).
54. X. Liu, J. Liu, D. Zhan, J. Yan, J. Wang, D. Chao, L. Lai, M. Chen, J. Yin, and Z. Shen, *RSC Adv.*, **3**, 11601 (2013).
55. L. Fu, G. Lai, G. Chen, C.-T. Lin, and A. Yu, *ChemistrySelect*, **1**, 1799 (2016).
56. L. Stagi, J. Ren, and P. Innocenzi, *Mater.*, **12**, 3905 (2019).
57. H. Hu, Z. Zhao, Q. Zhou, Y. Gogotsi, and J. Qiu, *Carbon N. Y.*, **50**, 3267 (2012).
58. L. Fan, Y. Zhou, M. He, Y. Tong, X. Zhong, J. Fang, and X. Bu, *J. Mater. Sci.*, **52**, 13522 (2017).
59. L. Fu, Z. Liu, Y. Huang, G. Lai, H. Zhang, W. Su, J. Yu, A. Wang, C.-T. Lin, and A. Yu, *J. Electroanal. Chem.*, **817**, 128 (2018).
60. M. Du, Y. Wu, and X. Hao, *CrystEngComm*, **15**, 1782 (2013).
61. M. Adeel, M. M. Rahman, and J. J. Lee, *Biosens. Bioelectron.*, **126**, 143 (2019).
62. Z. Tian, K. Chen, S. Sun, J. Zhang, W. Cui, Z. Xie, and G. Liu, *J. Adv. Ceram.*, **8**, 72 (2019).
63. N. Wang, G. Yang, H. Wang, C. Yan, R. Sun, and C.-P. Wong, *Mater. Today*, **27**, 33 (2019).
64. A. S. Nazarov, V. N. Demin, E. D. Grayfer, A. I. Bulavchenko, A. T. Arymbaeva, H. J. Shin, J. Y. Choi, and V. E. Fedorov, *Chem. Asian J.*, **7**, 554 (2012).
65. S. Angizi, A. Hatamie, H. Ghanbari, and A. Simchi, *ACS Appl. Mater. Interfaces*, **10**, 28819 (2018).
66. N. R. Glavin, M. L. Jespersen, M. H. Check, J. Hu, A. M. Hilton, T. S. Fisher, and A. A. Voevodin, *Thin Solid Films*, **572**, 245 (2014).
67. M. Sajjad and P. Feng, *Mater. Res. Bull.*, **49**, 35 (2014).
68. M. Rousseas, A. P. Goldstein, W. Mickelson, M. A. Worsley, L. Woo, and A. Zettl, *ACS Nano*, **7**, 8540 (2013).
69. W. Luo, T. Yang, L. Su, K.-C. Chou, and X. Hou, *RSC Adv.*, **6**, 27767 (2016).
70. Y. Zhang, *Int. J. Electrochem. Sci.*, **13**, 5995 (2018).
71. A. Nag, K. Raidongia, K. P. S. S. Hembram, R. Datta, U. V. Waghmare, and C. N. R. Rao, *ACS Nano*, **4**, 1539 (2010).
72. D. Velázquez, R. Seibert, H. Man, L. Spentzouris, and J. Terry, *J. Appl. Phys.*, **119**, 95306 (2016).
73. S. A. Vanalakar, G. L. Agawane, S. W. Shin, M. P. Suryawanshi, K. V. Gurav, K. S. Jeon, P. S. Patil, C. W. Jeong, J. Y. Kim, and J. H. Kim, *J. Alloys Compd.*, **619**, 109 (2015).
74. A. P. Caricato and A. Luches, *Appl. Phys. A*, **105**, 565 (2011).
75. A. Harley-Trochimczyk, T. Pham, J. Chang, E. Chen, M. A. Worsley, A. Zettl, W. Mickelson, and R. Maboudian, *Adv. Funct. Mater.*, **26**, 433 (2016).
76. Y. Shen, H. Yan, H. Guo, Y. Long, and W. Li, *Sens. Actuators B Chem.*, **303**, 127248 (2019).
77. Y.-S. Bi, B. Liu, X.-Y. Liu, Y. Qin, and B.-X. Zou, *J. Nanomater.*, **2020**, 1 (2020).
78. Y. Yang et al., *Appl. Catal. B Environ.*, **245**, 87 (2019).
79. S. Umrao, A. K. Maurya, V. Shukla, A. Grigoriev, R. Ahuja, M. Vinayak, R. R. Srivastava, P. S. Saxena, I. K. Oh, and A. Srivastava, *Mater. Today Bio*, **1**, 100001 (2019).
80. A. Krupa, M. Descamps, J.-F. Willart, B. Strach, E. Wyska, R. Jachowicz, and F. Danède, *Mol. Pharm.*, **13**, 3891 (2016).
81. S. Radhakrishnan et al., *Part. Part. Syst. Charact.*, **36**, 1800346 (2019).
82. A. Pakdel, Y. Bando, D. Shtansky, and D. Golberg, *Surf. Innov.*, **1**, 32 (2013).
83. M. Liu, Y. Xu, Y. Wang, X. Chen, X. Ji, F. Niu, Z. Song, and J. Liu, *Adv. Opt. Mater.*, **5**, 1600661 (2017).
84. A. Pakdel, C. Zhi, Y. Bando, and D. Golberg, *Mater. Today*, **15**, 256 (2012).
85. Q. Xue, H. Zhang, M. Zhu, Z. Wang, Z. Pei, Y. Huang, Y. Huang, X. Song, H. Zeng, and C. Zhi, *RSC Adv.*, **6**, 79090 (2016).
86. J. Yin, J. Li, Y. Hang, J. Yu, G. Tai, X. Li, Z. Zhang, and W. Guo, *Small*, **12**, 2942 (2016).
87. S. Azevedo, J. R. Kaschny, C. M. C. de Castilho, and F. de Brito Mota, *Eur. Phys. J. B*, **67**, 507 (2009).
88. M. Cheng, *J. Appl. Phys.*, **110**, 26106 (2011).
89. A. Merlo, V. R. S. S. Mokkapati, S. Pandit, and I. Mijakovic, *Biomater. Sci.*, **6**, 2298 (2018).
90. M. L. Yola and N. Atar, *Biosens. Bioelectron.*, **126**, 418 (2019).
91. M. L. Yola, *J. Mol. Liq.*, **277**, 50 (2019).
92. R. Zou, X. Li, G. Luo, Y. Niu, W. Weng, W. Sun, J. Xi, Y. Chen, and G. Li, *Electroanalysis*, **31**, 575 (2018).
93. M. K. Sharma, J. Narayanan, D. Pardasani, D. N. Srivastava, S. Upadhyay, and A. K. Goel, *Biosens. Bioelectron.*, **80**, 442 (2016).
94. H. Karimi-Maleh et al., *J. Mol. Liq.*, **310**, 113185 (2020).
95. V. Arabali, M. Ebrahimi, M. Abbasghorbani, V. K. Gupta, M. Farsi, M. R. Ganjali, and F. Karimi, *J. Mol. Liq.*, **213**, 312 (2016).
96. M. Nithya, *J. Biosens. Bioelectron.*, **06**, 1 (2015).
97. G. Elumalai, H. Noguchi, and K. Uosaki, *Phys. Chem. Chem. Phys.*, **16**, 13755 (2014).
98. K. Uosaki, G. Elumalai, H. C. Dinh, A. Lyalin, T. Taketsugu, and H. Noguchi, *Sci. Rep.*, **6**, 32217 (2016).
99. M. Khalaj, A. Sedghi, H. N. Miankushki, and S. Z. Golkhatmi, *Energy*, **188**, 116088 (2019).
100. S. Z. Golkhatmi, M. Khalaj, A. Izadpanahi, and A. Sedghi, *Solid State Sci.*, **106**, 106336 (2020).
101. L. Y. Jun, L. S. Yon, N. M. Mubarak, C. H. Bing, S. Pan, M. K. Danquah, E. C. Abdullah, and M. Khalid, *J. Environ. Chem. Eng.*, **7**, 102961 (2019).
102. G. Boczkaj and A. Fernandes, *Chem. Eng. J.*, **320**, 608 (2017).
103. S. K. Singhal, V. Kumar, K. Stalin, A. Choudhary, S. Teotia, G. B. Reddy, R. B. Mathur, S. P. Singh, and R. Pasricha, *Part. Part. Syst. Charact.*, **30**, 445 (2013).
104. Z. Wen, *Int. J. Electrochem. Sci.*, **12**, 4847 (2017).
105. M. Sawangphruk, Y. Sanguansak, A. Krittayavathananon, S. Luanwuthi, P. Srimuk, S. Nilmoung, S. Maensiri, W. Meevasana, and J. Limtrakul, *Carbon N. Y.*, **70**, 287 (2014).
106. C. H. Lee et al., *Adv. Mater.*, **25**, 4544 (2013).
107. C. Tang, Y. Bando, C. Zhi, and D. Golberg, *Chem. Commun.*, **44**, 4599 (2007).
108. C.-W. Chen, M.-H. Lee, and S. J. Clark, *Nanotechnology*, **15**, 1837 (2004).
109. N. A. Be, J. B. Thissen, S. N. Gardner, K. S. McLoughlin, V. Y. Fofanov, H. Koshinsky, S. R. Ellingson, T. S. Brettin, P. J. Jackson, and C. J. Jaing, *PLoS One*, **8**, 1 (2013).
110. H. Tomaso, C. Bartling, S. Al Dahouk, R. M. Hagen, H. C. Scholz, W. Beyer, and H. Neubauer, *Syst. Appl. Microbiol.*, **29**, 24 (2006).